LASER INTERFEROMETER GRAVITATIONAL WAVE OBSERVATORY
- LIGO -
CALIFORNIA INSTITUTE OF TECHNOLOGY
MASSACHUSETTS INSTITUTE OF TECHNOLOGY

Technical Document LIGO-T960134-00 - D 21 August 96

Alignment Sensing/Control Conceptual Design

Peter Fritschel, Gabriela Gonzalez, Daniel Sigg, Mike Zucker

Distribution of this draft:

ASC DRR Committee

This is an internal working note
of the LIGO Project.

California Institute of Technology
LIGO Project - MS 51-33
Pasadena CA 91125
Phone (818) 395-2129
Fax (818) 304-9834
E-mail: info@ligo.caltech.edu

Massachusetts Institute of Technology
LIGO Project - MS 20B-145
Cambridge, MA 01239
Phone (617) 253-4824
Fax (617) 253-7014
E-mail: info@ligo.mit.edu

WWW: http://www.ligo.caltech.edu/

1. ASC SUBSYSTEM: OVERVIEW

1.1. Interferometer System Context

The initial LIGO detector system (Figure 1) employs three power-recycled Michelson interferometers with Fabry-Perot cavity arms, each of length 2 km (at Hanford) or 4 km (at Hanford and Livingston). The main Core Optics (COC) components comprising each of these interferometers' optical systems are suspended as pendulums, mounted on seismic isolation stacks (SEI) within the vacuum envelope. They are illuminated by prestabilized laser light (PSL), which is phase modulated, filtered and mode-matched to the interferometer by a mode cleaner and other input optics (IOO). Light reflected from the core optics is shaped and directed by output optics telescopes and relay mirrors (COS) to fall on photodetection units of the Length Sensing and Control (LSC) system. The alignment of the optics to a common optical axis is achieved by the Alignment Sensing and Control (ASC) subsystem. Alignment is achieved by sequential use of initial alignment tooling and fixtures, optical lever systems, and beam centering units based on CCD cameras. The alignment is refined and maintained in normal operation by control systems which use wavefront sensors (ASC) acting through suspension actuators (SUS).

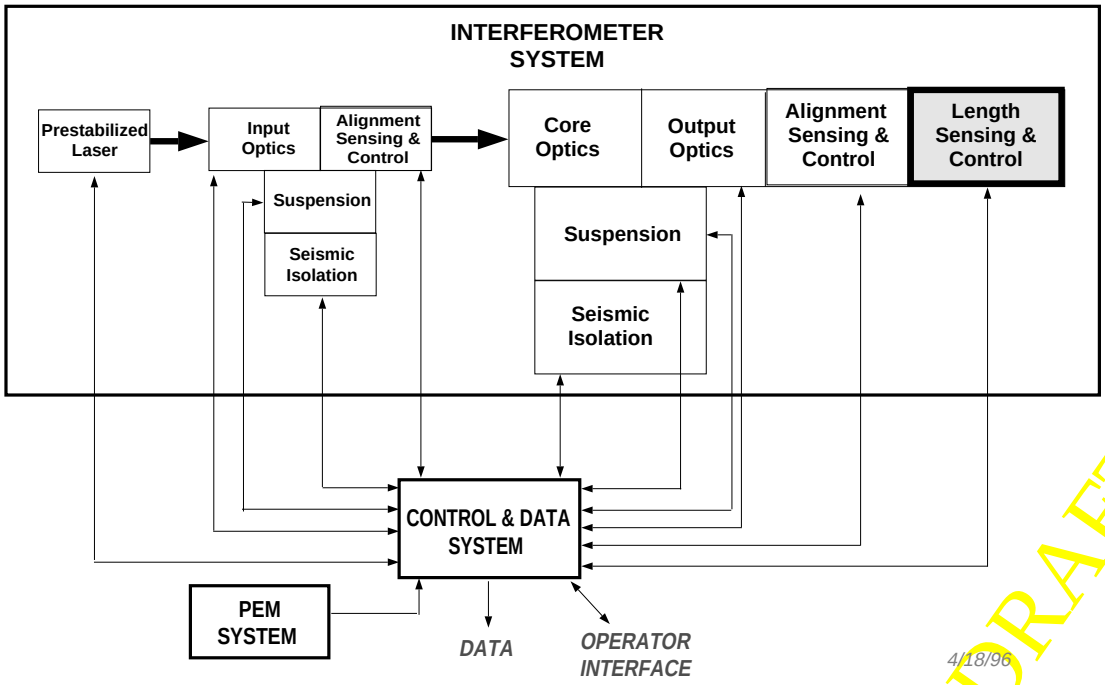

Figure 1 LIGO Detector subsystems

1.2. ASC modes of operation

The ASC subsystem is responsible for achieving and maintaining optical alignment in the interferometer. This is required so the laser light can become and remain resonant in the fundamental spatial mode of its cavities and be coupled efficiently into the interferometer, maximizing the circulating power (increasing the signal) and minimize the lost leakage power falling on the photodetectors (decreasing noise). To accomplish this, ASC must determine and control the two independent angular degrees of freedom of each core optic component (plus selected core optics support and input/output optics components). ASC must also provide the means for achieving alignment initially, including the provision of infrastructure for the installation of suspended optics inside the LIGO vacuum envelope, intermediate references for preservation of alignment through disturbances (such as pumpdowns), and means for converging adequate alignment for the Length Sensing and Control (LSC) subsystem to acquire resonance in the interferometer.

Functional requirements on the ASC subsystem are detailed in the *ASC Design Requirements Document* [1]. These requirements are categorized according to the various modes of ASC operation, from *initial alignment*, through *acquisition alignment* and finally *detection alignment* mode, the normal operating state for gravitational wave observations. In addition, ASC must provide *diagnostic and calibration* functions, both for its own operation and commissioning and to support diagnosis of other subsystems.

1.3. Dependencies and assumptions

1.3.1. COS beam delivery

It is assumed that all designated interferometer output beams and sample beams originating in vacuum:

- are fully collimated (waist position to lie within 2 m^{TBR} of exit vacuum I/O port)
- have Gaussian beam radii 2 mm^{TBR} < w < 4 mm^{TBR}
- exit vacuum I/O ports within +/- 5 cm^{TBR} of nominal IFO beam height
- exit I/O ports within 10 degrees^{TBR} of parallel to a horizontal ray perpendicular to the nominal IFO beam axis
- accumulate no wavefront aberrations exceeding $\lambda/10^{TBR}$ between the originating COC surface(s) and the exit interface.

1.3.2. IOO/LSC modulation

We assume that the IOO and LSC subsystems provide resonant and nonresonant phase modulation sidebands of the appropriate modulation indices, as detailed in Section 3.

1.3.3. LSC diagnostic operating mode for Acquisition Alignment

We assume that LSC will be able to support locking of a recycled short Michelson interferometer, as described in 2.2.2.

1.3.4. SUS control operation

We assume that SUS provides the means to exert torques on COC and other suspended optics controlled by the ASC system, through an electronic suspension actuator interface. Details of this interface are TBD (cf. LIGO-T950011, Suspension Design Requirements). We also assume the suspension damping performance is comparable to that described in LIGO-T960074-05-D, Suspension Preliminary Design, and that the local sensor noise is comparable to that described in reference [2]. The ASC Acquisition Alignment mode would be particularly vulnerable to long-term drift in suspension actuator bias currents and low-frequency current noise.

1.3.5. SEI performance and control operation

We assume that SEI provides the means to control the vertical and horizontal (transverse to the beam axis) position of the stack, through an electronic actuator interface. The range and resolution of control are assumed to be as laid out in the SEI DRD [5].

The design of the ASC alignment control loops in Detection mode will likely depend on the characteristics of the SEI stack transfer functions. The design presented in this document assumes stack performance comparable to that described in the SEI Conceptual Design [2]. Significant changes in the stack transfer functions may significantly alter the ASC control design (though no obstacles to meeting the ASC requirements are foreseen).

1.3.6. PSL power control

We assume that the PSL provides the means to modulate the laser power, as an aid in the initial alignment procedures, with roughly a 50% modulation depth at a rate of ~2 Hz. We also assume that the cw power level is adjustable, over the range given in the SYS DRD [1].

1.3.7. IOO control operation

We assume that the mode cleaner can be locked over the range of power levels given in section 1.3.6. Depending on the expectations of the mode cleaner stability, this may require length lock only, and not active alignment control.

2. INITIAL AND ACQUISITION ALIGNMENT

In the Initial Alignment mode, ASC will support the installation of suspended optical components within the vacuum envelope by providing pilot beams, optical lever references and specialized fixtures and tooling. These will allow installation of COC suspension assemblies with sufficient

accuracy to insure that additional adjustments performed during Acquisition Alignment will be within SUS actuator range (currently +/- 2 mrad; see LIGO-T950011, Suspension Design Requirements). Optical levers will be used as a transfer standard during installation and to monitor and (as necessary) maintain this state through the installation process, subsequent pumpdown, and operations. They also provide a semi-redundant alignment signal source for diagnostics and commissioning.

2.1. Installation Support

Installation of suspended components will require a coordinate system with a known relationship to the eventual interferometer beam axes. A coordinate system referenced to the facility foundations will be established and transferred to the internal mounting positions of the in-vacuum components via laser pilot beams and optical levers.

Initial Alignment will establish a coordinate system and an associated readout such that the equilibrium positions of suspended optics can be brought within 0.1 mrad of ideal alignment (thus within 10% of the SUS actuator range, which is the ASC requirement). The procedure outlined in sections 2.1.1.-2.1.4. below is summarized in the flow diagram in Figure 2.

2.1.1. Coordinate system initialization & Facility monument accuracy

Each facility building is provided with surveyed monuments whose absolute position has been marked and surveyed to allow placement of the vacuum equipment. The total transverse tolerance of the vacuum equipment placement with respect to the beam tube nominal axes is specified to be +/- 2.5 mm [9], indicating a maximum inclination of +/- 0.25 milliradian over the shortest equipment baseline (10 meters, at the end stations). We expect the monument positions themselves to be about a factor of two to five more accurate than this to allow the contractor some tolerance for the actual equipment placement. It should thus be possible to survey, using conventional and laser transits, a reference baseline in each station which is within +/- 0.1 mrad of parallel to each nominal beam tube clear-aperture axis.

2.1.2. Pilot beam setup

We will place a commercial laser transit at the end cover of HAM-1 and HAM-6 in the LVEA (or Adapter A-4 or equiv. in the midstation VEA, or BSC-9 or equiv. in the endstation VEA) and triangulate rays to 3 or more station alignment monuments within the LVEA/VEA. The laser transit is set to a height approximately 20 cm above nominal beam axis in nearby chambers, consistent with an available viewport on the cover, and is placed laterally to coincide with that viewport. After reducing the triangulation data, we reckon the best solution parallel to the beam tube axis, rotate the transit to this reading and lock it down. Its beam now threads through the vacuum system up to the BT termination gate valve. Two points are worth noting:

- The precision level on the transit or a long-baseline water level may afford pitch (altitude)

angle precision somewhat better than the yaw (azimuth) determined from the monuments.

- If schedule permits, even a brief test opening of the beam tube termination gate valves (for example, when the vacuum system is cycled “empty” for bakeout or leak testing) would allow sighting of the opposite station through the beam tubes. This could permit further refinement of the pilot beam direction. Subject to contractor schedule constraints, we may want to try and furnish pilot beam viewports and do some initial surveying during the VE installation phase.

These enhancements do not appear critical, but may significantly reduce the volume of alignment space addressed by the Acquisition Alignment mode; they will be investigated further in the Preliminary Design phase.

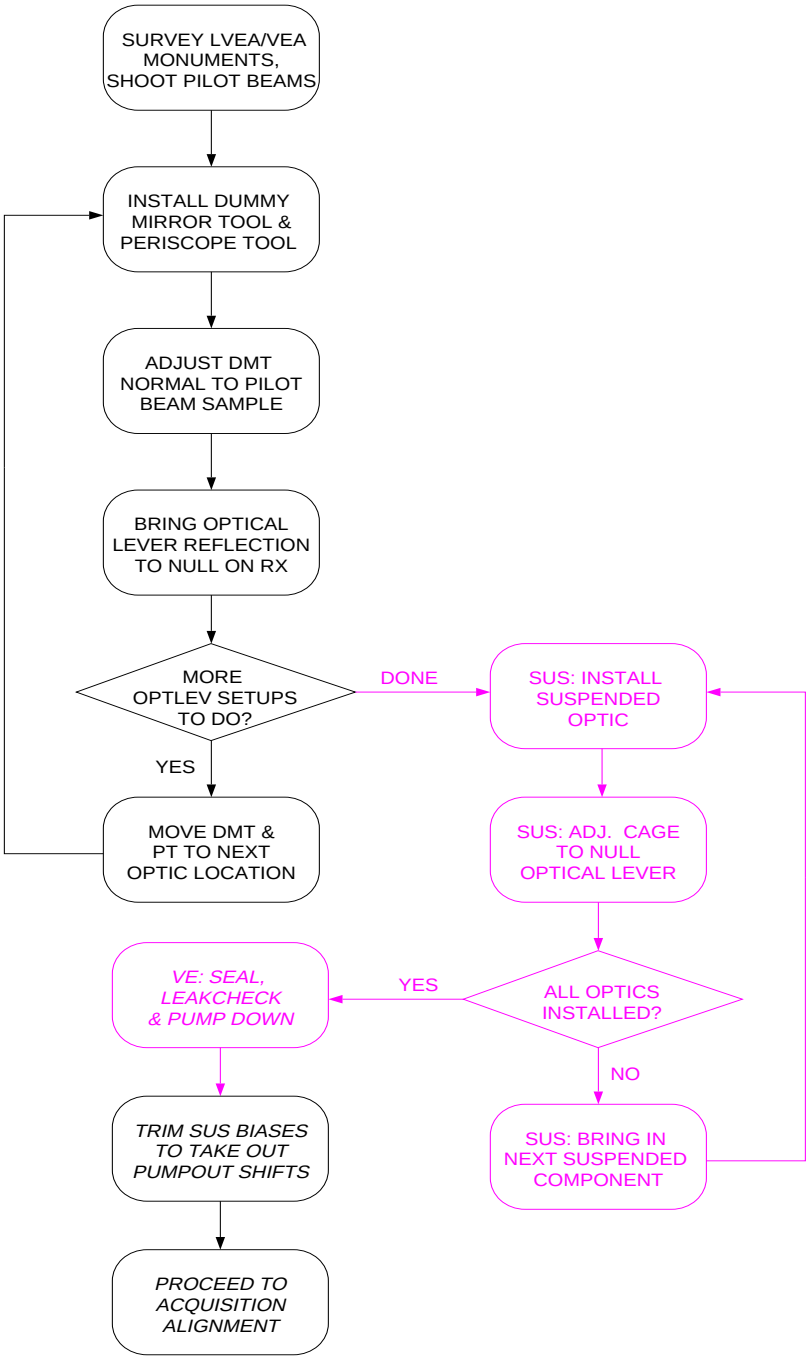

Figure 2 Procedure for establishing initial equilibrium alignment of suspended optics during installation. See text for discussion of tooling and fixtures.

2.1.3. Optical lever zero setting

With the vacuum envelope backfilled and opened, a kinematically-mounted “dummy” mirror (Dummy Mirror Tool, or DMT) is now installed in the position of a suspended optic. This stand-

in has the same beam axis height from the mounting plane as the corresponding suspended optic, and its first surface is translated axially to the design position. The pilot beam is sampled by a precision lateral transfer periscope (Periscope Tool, PT), which translates a sample of the pilot beam to the center of the DMT without introducing angular deviation (at the level of 10^{-4} rad). The DMT's kinematic mount is adjusted to retroreflect this beam back onto the pilot transit and locked, establishing the DMT as a local normal to the design beam axis.

To align the beamsplitter, pilot beam samples from both directions (originating at HAM-1 and HAM-6) will be brought to coincide spatially at the splitter's nominal first surface location using two PT fixtures. A Retro Reflection Tool (RRT, comprising a precision corner-cube retroreflector on adjustable-height mount) will be inserted in each transmitted beam; the DMT will then be adjusted to bring the right-arm retroreflection back onto the left-arm laser transit, and vice versa. (The RRT can also be used to reference the alternate surface of a normal-axis optic, if required.)

The suspended optic's optical lever transmitter (described below) is now played on the surface of the DMT, and the receiver pitch and yaw readouts are zeroed on this beam; the optical lever adjustments are then locked. The DMT and PT (and RRT if used) can now be removed. The process is repeated at each suspended optic location.

Optical lever readouts are subsequently used by the SUS installation team to set the suspensions in place (generally, only the yaw will be user-settable for the single-loop suspensions). In principle it will also be possible to use the PT to play a pilot beam sample directly on the suspended optic during installation and check for retroreflection (indeed, this may be a useful final checkout procedure), but sequential logistics and the clean readout provided by optical lever sensors probably make the transfer procedure outlined here more efficient.

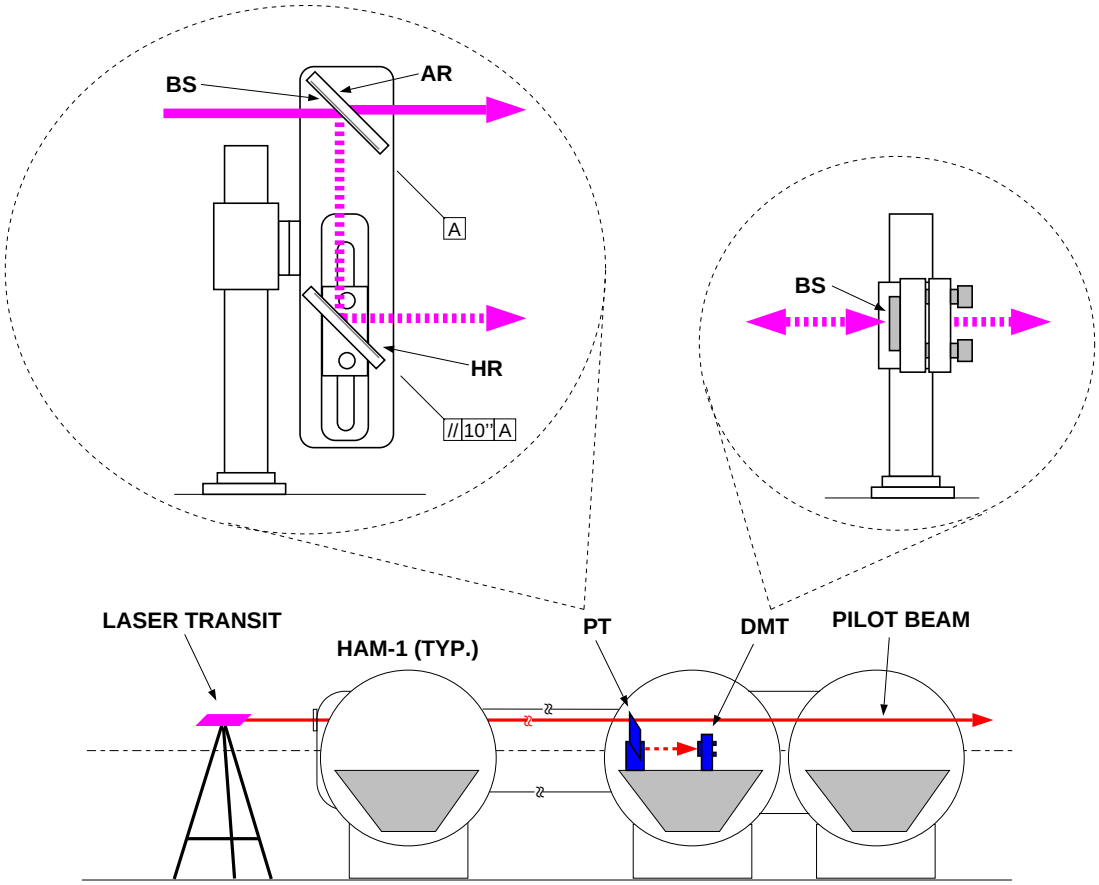

Figure 3 Pilot beam concept, showing dummy mirror tool (DMT) and periscope tool (PT). HR, BS, and AR denote high reflection, beamsplitter and antireflection coatings, respectively.

2.1.4. Initial beam direction zero

Once the recycling mirror, beamsplitter and ITM mirrors have been suspended and their directions adjusted to null the optical levers, the PSL and IOO mode cleaner will be brought to resonance and aligned at low power. Initial beam steering mirrors will then be manipulated to achieve centering on and retroreflection from the recycling mirror. The weak leakage beam transmitted by the recycling mirror is then used to align the dark port output optics, beam pickoffs, and external photodetector beam steering. These will be monitored throughout subsequent alignment stages and re-optimized as needed.

2.2. Transition to Acquisition Alignment

The task of achieving the Acquisition Alignment mode requires a procedure for moving from the initial equilibrium alignment (achieved at the end of the procedure given in Figure 2) to the degree of alignment necessary for LSC acquisition, and a method of maintaining this alignment in the Acquisition Alignment mode.

The system will seek and locate the optimum alignment through an iterative procedure, using the optical levers and/of the suspension local sensors for fiducial reference, and passing a succession of discrete bias torque updates to each SUS controller and/or SEI stack actuator controller. The seek algorithm will be repeated whenever the interferometer has remained inactive for long enough (TBD) that the angular range for LSC acquisition has been exceeded. Whenever the LSC acquires and Detection mode alignment and centering have converged, the resulting “perfect” alignment information will be used to update the optical lever and suspension bias references. Subsequent acquisition attempts will thus start from the last verified alignment state. The procedure outlined in this section for achieving acquisition alignment is presented in a flow diagram in Figure 5.

Since the expected alignment fluctuations in both the transition state and the Acquisition Alignment mode are critical inputs to the design, we discuss these first.

2.2.1. Angular control and fluctuations

Extensive modeling has been done of the angular fluctuations of a suspended optic under the control of the suspension’s local sensor. This modeling is discussed fully in reference [6], and in condensed form in Appendix 3. The main results relevant here are contained in Figure 4. This shows the rms angle fluctuations - relative to an inertial frame - in a bandwidth of (f_{lower} - 10 Hz). The horizontal axis of the figure, labelled *integration time*, is the reciprocal of f_{lower}. The curves in the figure thus indicate the rms angle excursion from some initial angle in a time span of *integration time*, as a function of the *integration time*. Two types of servos were used in the modeling, both using the suspension’s local sensor as input. Velocity damping is the traditional local servo; the modified servo includes more gain at frequencies below the suspension’s pitch/yaw eigenfrequencies. Details of these servos are given in Appendix 3. The ground noise used to drive the models comes from measurements at the two sites - details are given in Appendix 3.

Figure 4 predicts that we can attain a pitch angle stability of 10^{-7} rad rms over a timescale of 100 seconds (possibly longer - 100 seconds is the longest time scale of the current modeling results) at either site. At Livingston, the modified local servo is required due to the much larger microseismic peak amplitude; it gives roughly a factor of 5 improvement (over velocity damping) for time spans more than a couple of seconds. This level of stability is a factor of 5 smaller than the current estimate (and requirement) for the alignment tolerance in the Acquisition Alignment mode.

It is also possible to use the optical lever signals as the inputs to the local servos during the transition and Acquisition Alignment modes. This configuration will be further studied in the prelimi-

nary design phase, though in any event the design will include the option for the local servos to switch between the two types of sensors (see also section 6.1.).

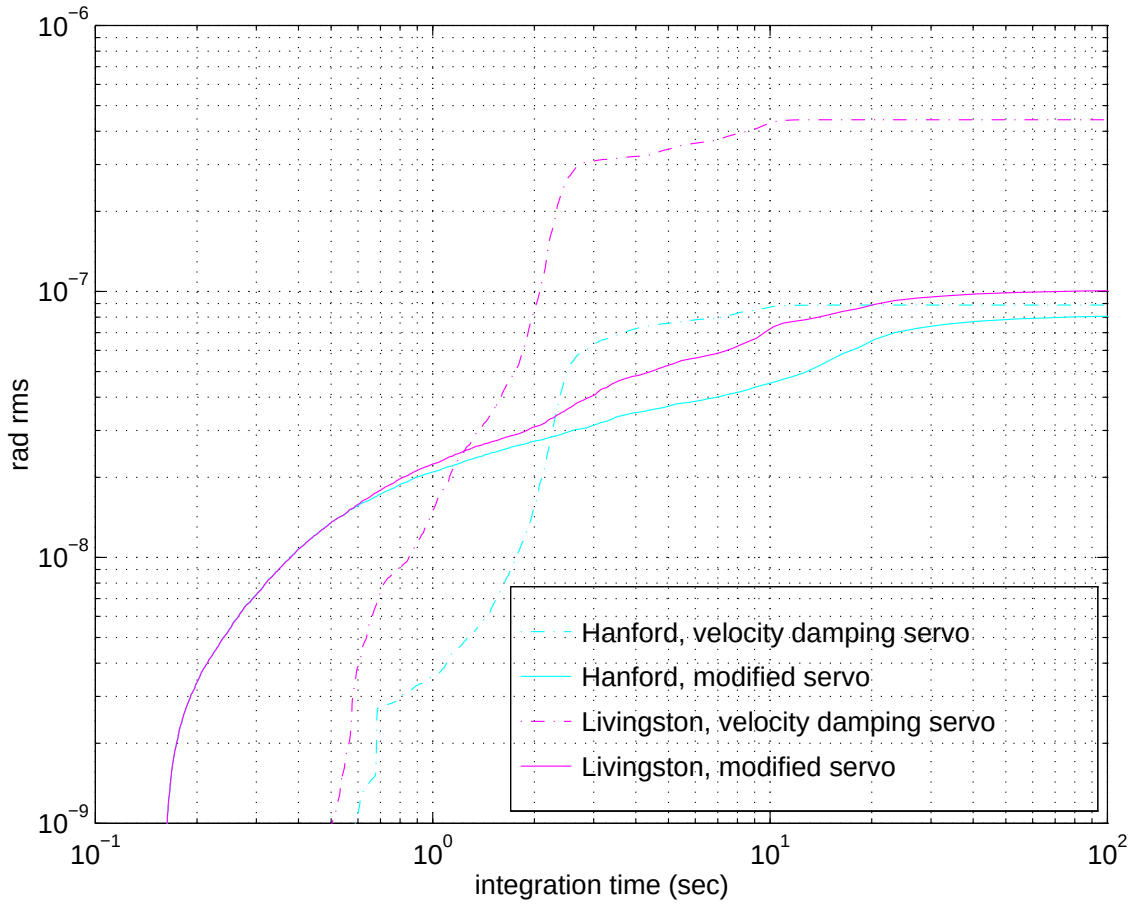

Figure 4 Pitch angle fluctuations of a suspended optics under local sensor control. See text for definition of servo types; 'Hanford' and 'Livingston' refer to the source of the ground noise used in the model. The 'integration time' is the reciprocal of the lower cut-off frequency of the integral which computes the rms angle (see text for further explanation).

2.2.2. Initialization: resonating the recycled short Michelson

The suspension control/damping systems will first be adjusted to restore the suspended optics back to the positions referenced by their local sensors or optical levers, in case pumpdown or stack drift has induced errors with respect to the original installation alignment. Although too coarse for resonance of the full interferometer, initial alignment should be adequate to achieve interference in the short Michelson subset. For this phase of the procedure, the ETM mirrors will be deliberately misaligned to avoid confounding reflections. The LSC modulation system is not optimized for this mode of operation, since the sidebands are not resonant without the phase shift

of resonating arm cavities; still, sufficient sideband amplitude will leak into the recycling cavity to obtain a small differential Michelson signal at the dark port.

The differential and common-mode LSC loops will be engaged in acquisition mode (with RF phases and gains selected appropriately for the abnormal topology). Fringe signals will guide iteration of the two ITM mirrors to optimize contrast (analogous to the differential-mode alignment procedure for the PNI prototype). Input steering mirrors will be adjusted to optimize common-mode alignment.

When satisfactory stable resonance is achieved, a differential-mode (DM) optimization routine will iteratively converge the optimal angles for each ITM mirror, and the translations and angles of the input beam steering will be similarly converged by a common-mode (CM) alignment optimizer. The optical lever signals will be stored and the optical levers re-zeroed at the new location.

Alternatively we may choose to invoke the wavefront sensing system (see section 3.2.1.) to automatically maintain optimum alignment of the short-arm recycled Michelson - at least for some of the alignment degrees-of-freedom. It appears feasible to accommodate this particular configuration by changing WFS system loop gain and demodulation phase to compensate the loss of sideband resonance in the recycling cavity. This option will be further explored in the preliminary design phase.

2.2.3. Scan search: on-line beam

The beam centering cameras (see 4.2.2. below) at the endstations or midstations are set to observe the scattered light from the interior back wall of the BSC chamber. The arm carrying the on-line beam (the beam transmitted by the beamsplitter) will be monitored first.

The leakage field through the ITM from the resonating recycled Michelson will produce a transmitted beam up to several watts in power (about half the incident laser power goes down each beam tube; it may be desirable to operate at very low power to avoid overloading). The laser power is modulated (~ 50% depth, 2 Hz) to help distinguish scattered laser light from ambient illumination. Assuming no sign of the transmitted field appears in the on-line ETM chamber, the recycling mirror is rotated by a small increment, about 0.03 mrad, moving the beam about 1/4 the angle subtended by the tube clear aperture. (It is probably moved initially in yaw, given the higher uncertainty of that initial setting). The DM and CM optimization procedures are then invoked to restore ITM and input beam alignment to this new recycling mirror angle, again maximizing the circulating power in the Michelson. Assuming no transmitted beam is detected in the on-line ETM chamber, the process is repeated, stepping out a search pattern (whose limits are determined by the estimated error budget of the Initial Alignment). At each iteration the optical lever readouts are stored and their zeros are updated.

To estimate how long this procedure will take, note that the solid angle subtended by the initial alignment error box should be comparable to that subtended by the tube clear aperture. The transmitted beam should thus be found in the first few iterations.

When the transmitted beam is located in the end chamber (or sufficient scattered light is imaged to form an unambiguous interpretation of the error), the beam centering system measures the centroid's offset with respect to the ETM and interpolates the ETM center. The recycling mirror normal is commanded to meet this point, and the CM and DM optimizers follow suit, bringing the ITM and input beam angles into agreement. The beam is now transmitted through the ETM and picked up by the transmitted-light centering monitor (there will be plenty of power, but attenuators normally used to protect this monitor may have to be disabled). A final iteration of the recycling mirror angle and optimization of the CM and DM alignment complete this phase.

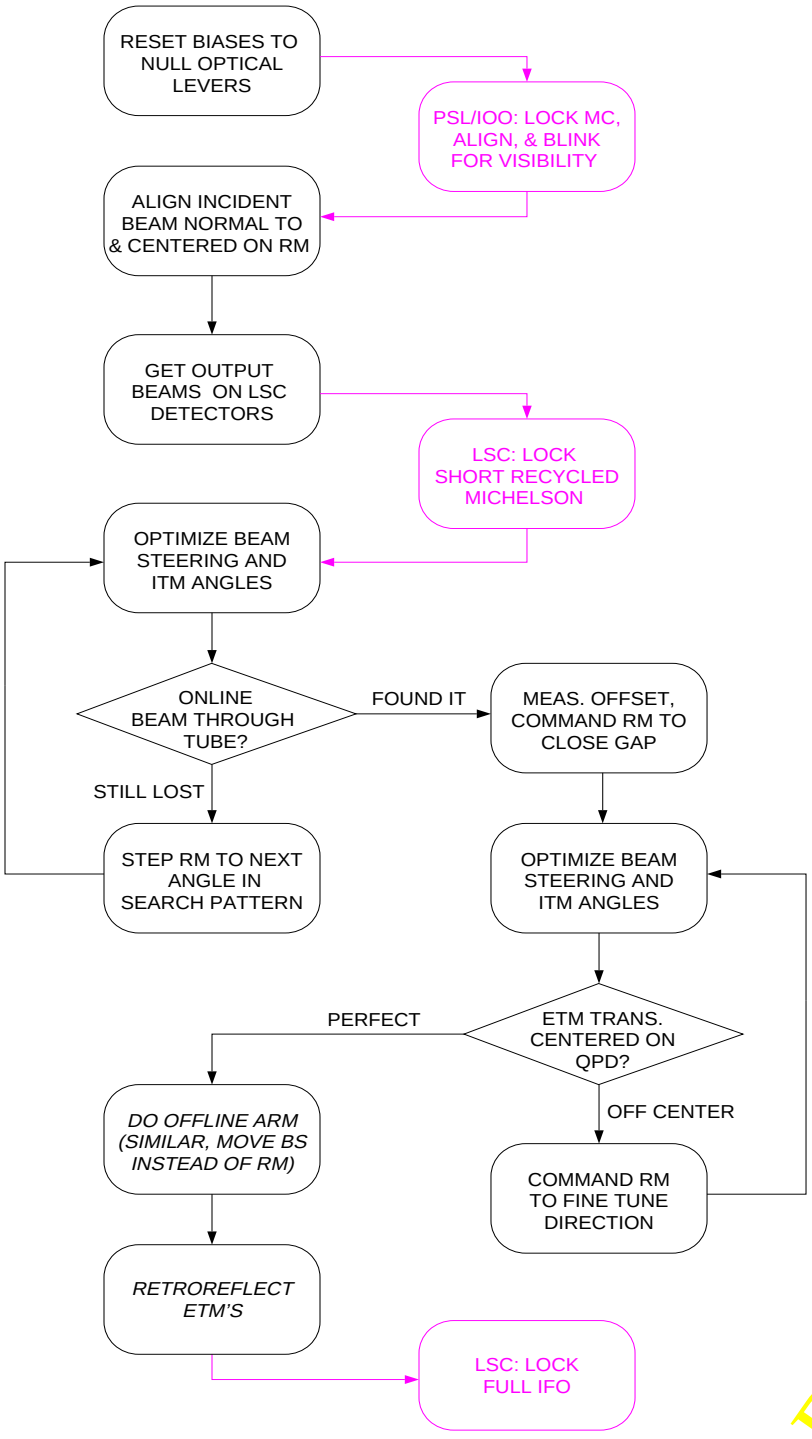

Figure 5 Procedure for achieving acquisition alignment after pumpdown or other major disturbance

2.2.4. Scan search: off-line beam

An analogous procedure is next performed for the off-line beam, but in this case the beamsplitter angle is stepped with each iteration rather than the recycling mirror. The optimization will be somewhat simpler, since only DM motions should be affected by each step. In the end state, the beam in the off-line arm hits center on the off-line ETM.

2.2.5. Retroreflection of the ETM's

Switching the centering cameras to monitor the scattered light from the inside walls of the ITM BSC chambers (and possibly HAM chambers or beam tube manifold reducers), each ETM is scanned to bring its reflection back to the vertex. Although this should be straightforward (a simplified subset of the above two procedures), some time-saving convergence aids may be employed[1]. With the retroreflected beam located, it is moved to a distinctive target (e.g., a beam-dump) in the ITM chamber whose offset from the suspended mirror axis is precisely known. From this baseline, the ETM can be repointed to bring the beam back on the ITM in a single step with repeatability of a few mm^{TBR}. The neutral "resting" position will also be useful for further alignment iterations or for diagnostics requiring misalignment of the ETM.

3. DETECTION ALIGNMENT & CENTERING

3.1. System configuration

Figure 6 shows a block diagram of the Alignment System in Detection Mode. The ten mirror alignment degrees-of-freedom are sensed with wavefront sensors (WFS 1 ... WFS 5), which are detecting a sample of the interferometer beam at various ports in the interferometer. Five (two-dimensional) independent sensor signals are needed to detect all degrees-of-freedom. One of the sensor heads shown actually produces two independent signals (in orthogonal rf phases), so that one of the sensor signals in the system is redundant. We include this in the design as an alternative sensor for the alignment control, and/or as a diagnostic sensor.

An individual wavefront sensor signal is proportional to combinations of misalignments of the interferometer mirrors; thus the signals from all the wavefront sensors are first processed together to determine the alignments of the individual mirrors. The resulting alignment information is the ALIGNMENT DATA.

1. For example, introduction of an external corner-cube retroreflector in the ETM transmitted beam provides a return pilot beam colinear with the cavity axis; adjusting the ETM normal to it by monitoring its back-reflection will automatically achieve the desired result. Also, given sufficient geometric accuracy and linearity, one may introduce a series of large misaligments, accurately note positions where the ETM's reflection strikes the local vacuum envelope walls, and interpolate the centerline.

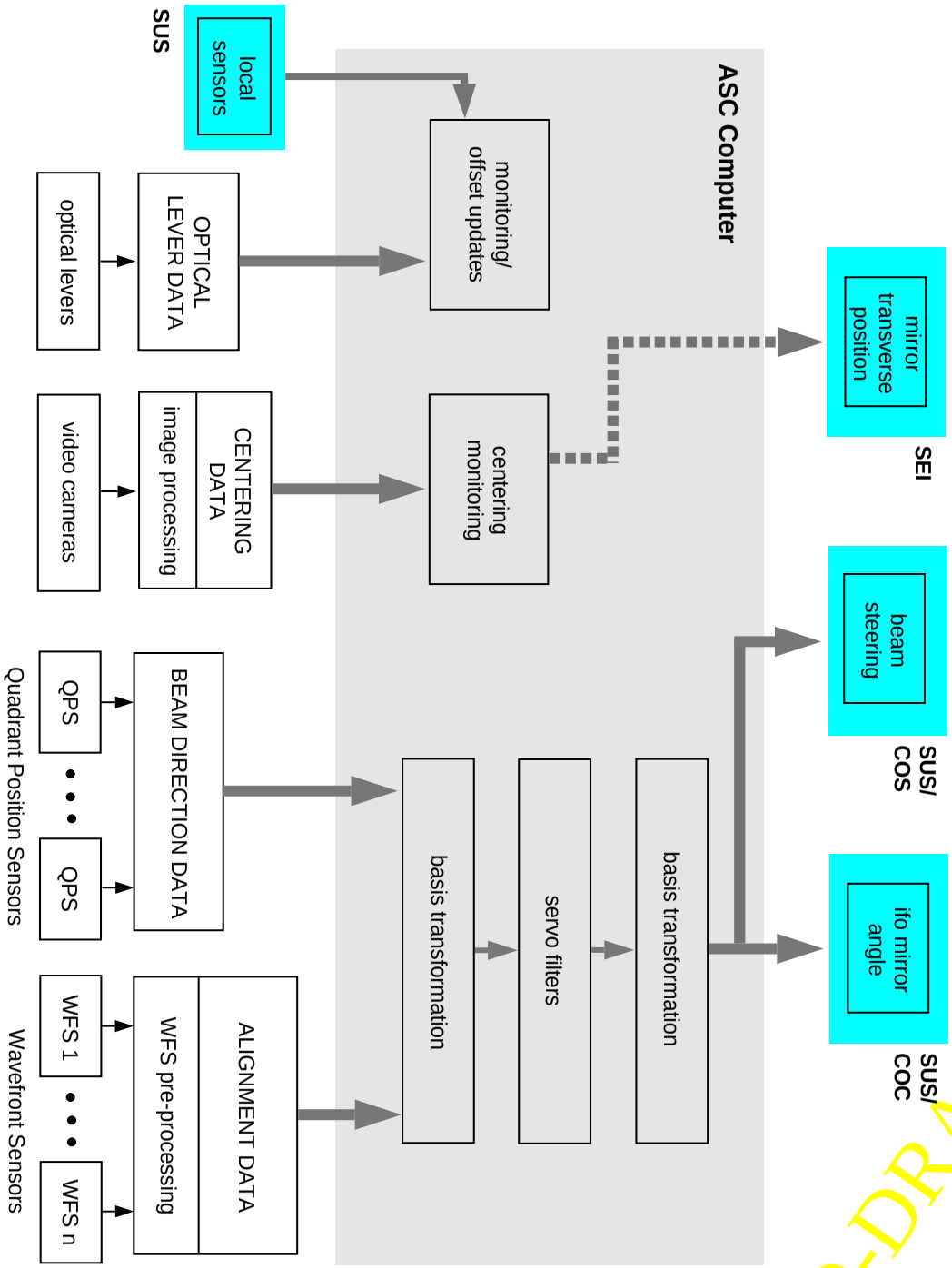

Figure 6 Block diagram of Detection Mode Alignment System. The dashesd line between 'centering monitoring' and 'mirror transverse position' indicates that there is no active control of the transverse position.

The beam centering on the test masses is monitored in several ways. The beams transmitted by the ETM mirrors are monitored with position sensitive photodetectors, affixed to the facility foundation by demountable platforms (Figure 18). All reflected beams sampled by ASC wavefront sensors are also sampled by position-sensing monitor diodes (this is deliberately somewhat redundant with the readout provided by WFS DC outputs). The information from these position sensors gives the BEAM DIRECTION DATA.

The beam locations on all COC optics are monitored with cameras which detect the scattered light from the optics, giving the CENTERING DATA. Illuminators will be provided to increase the visibility of the core optic edges, permitting accurate coordinate measurement with respect to the body itself. This permits noncritical mounting of some cameras directly to the vacuum envelope in areas where an external optical platform is not conveniently available.

The centers of rotation of the test masses are initially determined by modulating the pitch and yaw orientations of each test mass, and minimizing the coupling of angle modulation to length modulation.

The ALIGNMENT DATA and the signals from the centering sensors are processed together to transform the signals to a matrix of error signals for the individual mirror angles and the input beam direction. The appropriate servo loop filtering functions are applied to these error signals; they are then transformed into the appropriate control basis and sent to the orientation inputs of the SUS controllers of the COC (for interferometer mirror angles) and COS (for input beam direction) optics. Centering adjustments which would require transverse motion of the seismic isolation stacks are done as part of diagnostic/monitoring only, and not with a closed loop servo control.

3.2. Sensing conceptual designs

3.2.1. Wavefront Sensing

3.2.1.1 General description

The wavefront sensor technique makes use of the phase modulation that is impressed on the light to generate the length control error signals. The detection of misalignments is quite similar to the detection of length deviations, with the addition that the light is spatially detected. If the interferometer is misaligned, the higher-order transverse modes excited can be detected by measuring the amplitude modulation on a segmented photodetector. For small misalignments, the error signal arises from the interference of the TEM_{00} mode of the carrier (sideband) with the $TEM_{10/01}$ mode of the sideband (carrier). An additional degree-of-freedom (not present in the length detection) comes from the fact that different higher-order modes propagate with different Guoy phases; the detected signal thus depends on the distance between the photodetector and the interferometer

port. This distance (phase) can be controlled with a telescope. Because this technique detects the existence of $TEM_{10/01}$ modes, it does not require an external reference frame (which would have the potential to drift relative to the interferometer).

3.2.1.2 Optical signal generation

The generation of $TEM_{10/01}$ modes in the interferometer by tilts of the mirrors has been modeled with the modal decomposition model [3]. The base parameters of the interferometer used in the model are given in Table 9 in Appendix 1. The WFS signals produced by the interference of TEM_{00} and $TEM_{10/01}$ modes are computed at four ports of the interferometer: the **dark port**; the **reflected port** (the light reflected from the interferometer); the **recycling cavity port** (a sample of the light traveling toward the beamsplitter); the **arm reflection port** (a sample of the light reflected from the on-line arm cavity - taken in practice from the beamsplitter AR surface reflection). At each port there are two controllable variables which further determine the signal from a WFS - the Guoy phase η_{guoy} between the TEM_{00} and $TEM_{10/01}$ modes, and the phase of the rf-signal (with respect to the phase of the impressed phase-modulation) produced by the beating of the carrier and sidebands (in general a WFS signal is produced by the interference of a carrier TEM_{00} mode with a sideband $TEM_{10/01}$ mode, and/or the interference of a carrier $TEM_{10/01}$ mode with a sideband TEM_{00} mode). Figure 7 shows the port locations and a functional block diagram of a generic WFS (head + demodulator).

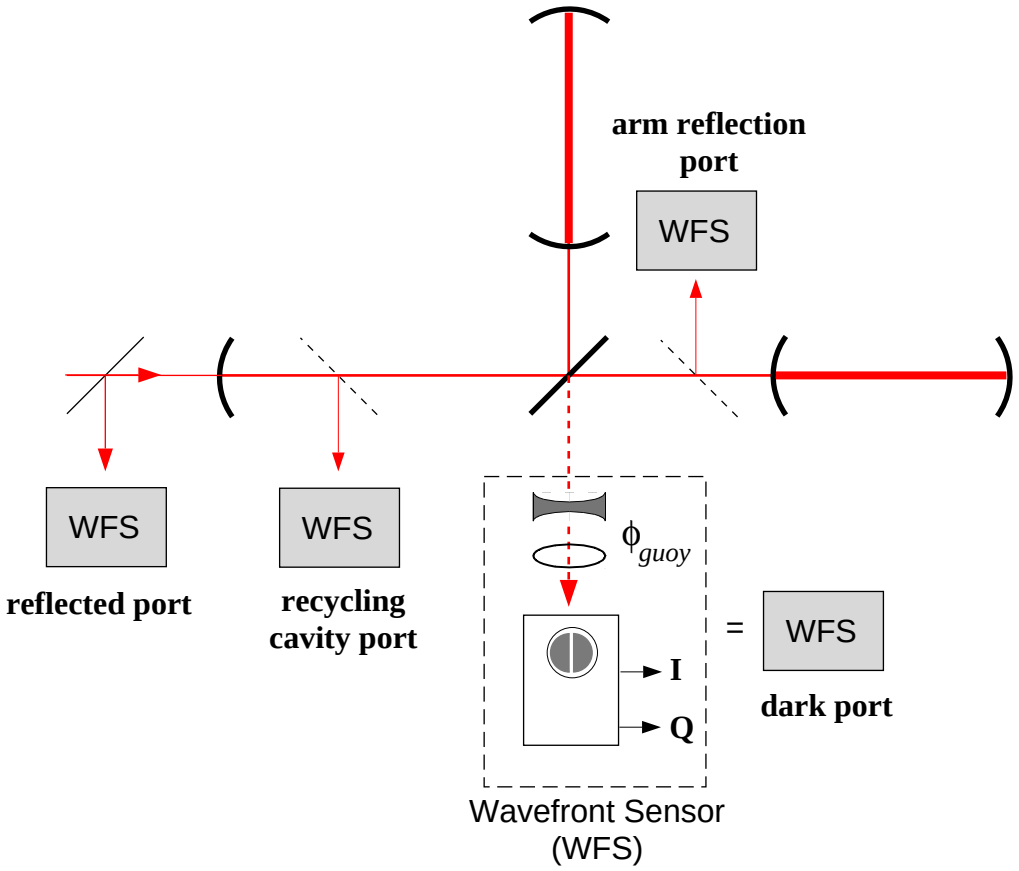

Figure 7 Illustration of interferometer fields and detection variables used in the wavefront sensor signal calculations. The splitters are figurative, and represent beams from AR surfaces.

At a particular port the wavefront sensor signal in general depends on all five degrees-of-freedom (in one dimension), and it can be written as:

$$WFS(\phi_d, \phi_g, \Theta, \Gamma) = P f(\Gamma) f_{\text{split}} k_{PD}^{10} \sum_{i=1}^{5} A_i \Theta_i \cos(\eta - \eta_{0i}) \cos(\omega_m t - \phi_{0i}) \quad (1)$$

where for the *i*th angular d.o.f., Θ_i is the normalized misalignment angle[1], η_{0i} is the Guoy phase at the output port, η the Guoy phase shift added by the WFS telescope, ϕ_{0i} the phase of signal at the modulation frequency ω_m. The coefficient A_i is the rf-modulated component of the optical intensity due to the interference of TEM_{00} and TEM_{10} modes, integrated over a half-plane detector[2]. The units of A_i are watts, and it is normalized to 1 W of total input power; the modulation index is

1. Normalized to the beam divergence angle: $\Theta_i = (\pi\omega_0/\lambda)\theta_i^{\text{real}}$.
2. A half-plane detector is one that subtracts and integrates over two mirror-symmetric half-infinite planes located left and right of the *y*-axis.

incorporated in the factor $f(\Gamma) \equiv 2\,J_0(\Gamma)\,J_1(\Gamma)$, which for low modulation index reduces to $f(\Gamma) \approx \Gamma$ (A_i is independent of the modulation index). The input power is *P,* the fraction of a particular port's light that is directed to the wavefront sensor is f_{split}, and k_{PD}^{10} is a less-than-unity factor which accounts for the difference between the specific photodiode geometry and the idealized half-plane detector.

In addition to the WFS signals produced by the TEM_{00}/TEM_{10} modes of the carrier and sidebands, the signals produced by the carrier and another set of non-resonant sidebands have also been computed. These non-resonant sidebands do not meet any of the resonance conditions in the interferometer, and are essentially completely reflected from the recycling mirror and are not perturbed by any of the other degrees-of-freedom of the interferometer. These extra sidebands have been included in order to be able to separate misalignment of the recycling mirror from common misalignment of the input test masses.

	Angular Degree-of-Freedom									
Port	**ΔETM**		**ΔITM**		**$\overline{\text{ETM}}$**		**$\overline{\text{ITM}}$**		**RM**	
Dark	**-21.0**		**-9.62**		8.2×10^{-6}		3.7×10^{-6}		6.8×10^{-4}	
	Q	90°	Q	90°	Q	18°	Q	10°	Q	90°
Reflected	3.6×10^{-2}		**-2.16**		-0.23		**12.22**		**-17.08**	
	Q	35°	Q	35°	I	-44°	I	36°	I	35°
Recycling cavity	-5.1×10^{-3}		**-0.310**		4.9×10^{-2}		**1.75**		**-2.422**	
	Q	35°	Q	35°	I	-61°	I	36°	I	35°
Arm reflection	-6.0×10^{-2}		**0.160**		2.5×10^{-2}		**0.894**		**-1.245**	
	Q+5°	-90°	I-12°	36°	Q+5°	-61°	Q+5°	36°	Q+5°	35°
Reflected - NR sideband	7.8×10^{-5}		-5.8×10^{-4}		**-2.16**		**-0.983**		**1.97**	
	I+5°	1°	Q+4°	0°	I	90°	I	90°	I	0°

Table 1 Matrix of Wavefront Sensor signals. Top entry in each cell is A_i (with significant values in boldface), lower-left is rf-phase, and lower-right is the Guoy phase.

The matrix of WFS signals generated by the interferometer defined in Table 9 is given in Table 1. In each cell of the table, the top entry is A_i, the lower-left is the rf-phase (I and Q referring to in-

phase and quadrature-phase), and the lower-right is the Guoy phase η_{0i} The A_i for the recycling cavity and arm reflection ports include a factor of 10^{-3}, representing the (expected upper limit) reflectivity of the sampling surfaces for these ports.

There are some comments to be made on this matrix:

- the interference between the carrier and the non-resonant sideband provides a separation in Guoy phase between the recycling mirror and the common mode input test mass (there is no separation in the carrier-resonant sideband interference terms, due to the degeneracy of the recycling cavity)
- among the carrier-resonant sidebands signals, the common end test mass signal is always much smaller (factor of 30-50) than the common input test mass signal (though they are separated in Guoy phase); this is because there is a buildup of the resonant sideband TEM_{10} mode in the degenerate recycling cavity in the presence of a common input test mass misalignment; these degrees of freedom are thus hard to separate even though there is a Guoy phase separation - a factor of ten suppression of the common ITM signal by adjustment of the Guoy phase still leaves it being several times bigger than the common ETM signal
- the carrier-non-resonant sideband signals do give a better measure of the common ETM signal (at a Guoy phase 90° from the optimal recycling mirror Guoy phase); here the common ITM and ETM signals have the same optimal Guoy and demodulation phases, but the common ETM signal is ~2 × bigger than the common ITM
- the carrier-non-resonant sideband recycling mirror signal relies on the existence of a carrier TEM_{00} field at the reflection port; the interferometer should thus not be critically, or too close to critically, matched
- the differential ETM mode has a reasonable separation only at the dark port, where it is ~2× bigger than the differential ITM (though they are degenerate in Guoy and demodulation phases)
- the signals from the reflected, recycling cavity, and arm reflection ports give nearly the same information; i.e., these vectors are nearly co-linear

Dependent degrees-of-freedom. The WFS system is capable of detecting only five independent degrees-of-freedom; these were selected to be those of the test masses and the recycling mirror, and the WFS signals produced by a misaligned beamsplitter or tilted or shifted input beam were not calculated. These degrees-of-freedom can be expressed as linear combinations of the recycling mirror and test mass angles, as follows:

$$\begin{aligned} \theta_{BS} &= 0.92\,\theta_{ETM2} - 2.01\theta_{ETM2} - 0.01\theta_{RM} \\ IB_{tilt} &= -0.652\,\overline{\theta_{ETM}} + 1.431\,\overline{\theta_{ITM}} + 1.01\theta_{RM} \\ IB_{shift} &= -(0.508\,\overline{\theta_{ETM}} + 0.767\,\overline{\theta_{ITM}} + 0.542\theta_{RM})\frac{\omega_0}{\theta_0} \end{aligned} \tag{2}$$

where IB denotes the input beam, ω_0 is the beam waist size, and θ_0 is the beam divergence angle (in the arm cavity). These relations follow directly from the geometry of the cavities.

3.2.2. Beam Centering

3.2.2.1 Centering degrees-of-freedom

The WFS system gives no information about the position of the laser beam on the COC optics. The ASC must control these centering degrees-of-freedom (d.o.f.) such that the beam centroids are within 1 mm of the center-of-rotation of the test masses, and within 5 mm of the nominal beam location for the beamsplitter and recycling mirror.

The effects of angular misalignments of the COC optics and the input beam on the beam positions in the interferometer can be calculated geometrically, and are shown in Figure 2.

mirror or port	angular degree-of-freedom							
	ΔETM	ΔITM	$\overline{\text{ETM}}$	$\overline{\text{ITM}}$	RM	BS	IB_{tilt}	IB_{shift}
dark port	$< 10^{-4}$	$< 10^{-2}$	0.338	–20.2	28.4	28.9	–0.517	0.940
reflected	$< 10^{-4}$	$< 10^{-3}$	6.36	–5.63	11.9	12.1	–0.217	–4.34
recycling	$< 10^{-4}$	$< 10^{-4}$	1.10	–1.63	2.96	3.02	–0.054	0.083
ITM1	–1.16	–0.527	1.17	0.532	$< 10^{-2}$	$< 10^{-3}$	$< 10^{-3}$	$< 10^{-3}$
ITM2	1.16	0.527	1.17	0.532	$< 10^{-2}$	0.011	$< 10^{-3}$	$< 10^{-3}$
ETM1	–0.845	–1.16	0.845	1.16	0.013	$< 10^{-3}$	$< 10^{-3}$	$< 10^{-3}$
ETM2	0.845	1.16	0.845	1.16	0.013	0.026	$< 10^{-3}$	$< 10^{-3}$

Table 2 Matrix of beam center sensitivity. All numbers are in units of waist size per divergence angle of the arm cavity.

The WFS system will act to stabilize the first five degrees-of-freedom to 10^{-8} radians or better. The beam position fluctuations on the test masses due to these d.o.f. would then be on the order of 0.05 mm, much smaller than the centering requirement. We can thus consider that the WFS system nulls out the effects of these d.o.f. on the beam centering.

The effects of the remaining d.o.f. can then be determined by measuring the beam position at three suitable points in the interferometer. We choose these points to be the light transmitted by each of the end test masses and the light reflected from the interferometer. The matrix of beam center position at these ports as determined by the beamsplitter and input beam d.o.f. is given in Table 3.

The measurements provided by the WFS system and the quad cell monitors are sufficient to ensure proper centering if the centers of the suspended optics remain on the lines determined by the initial beam axes. But drifts in the seismic isolation stacks are expected to take the optics off

port	BS	IB_{tilt}	IB_{shift}
reflection	–0.033	–0.011	1.02
transmission ETM_1	0.019	–1.12	1.33
transmission ETM_2	2.46	–1.12	1.33

Table 3 Centering Matrix. The values are in units of arm cavity waist size per arm cavity divergence angle (for BS and IB_{tilt}) or per arm cavity waist size (IB_{shift}).

of these lines by an amount comparable to or larger than 1 mm over a time scale of several months or more [5].

In order to monitor the effects of such drifts, CCD cameras will be used to determine the position of the cavity beam on the test masses. These cameras will be mounted external to the vacuum system and will detect the light scattered from the test masses. The position of the optic's image on the camera will be determined by illuminating the optic with a light source (external to the vacuum - supplied by ASC).

3.2.2.2 Establishing centers-of-rotation

In order to initially determine the centers of rotation of the optics, the pitch and yaw orientation of the test masses, the beamsplitter and the recycling mirror will be sequentially modulated. The signals produced at the gw output by the test mass and beamsplitter angular modulations, and at the arm common output by the recycling mirror modulation, are processed to determine the beam offsets on the optics. Corrections are then made to the input beam angle and position and the beamsplitter angle; if the magnitude of correction requires it, the stack coarse actuators will be used to make the necessary transverse displacements. The dithering routine is then repeated to check that the centering requirement for all optics has been met. Figure 8 shows a flow diagram of this routine.

The frequency and amplitude of modulation should be such that the measurements can be made quickly and with high S/N. The modulation frequency will be in the gw-band - most likely between 50 and 100 Hz. An amplitude of 10^{-10} radians rms is small enough that power levels in the interferometer are unaffected. Coupled with a beam offset of 1 mm, this would produce a length signal of 10^{-13} m rms, which is several orders of magnitude above the interferometer displacement noise in a 1 Hz bandwidth above 50 Hz. The angle-length coupling for all test masses could thus be measured in a few seconds. This angular dithering routine can also be performed as a diagnostic at any time (and can also serve to calibrate the WFS signal matrix, see section 5.4.).

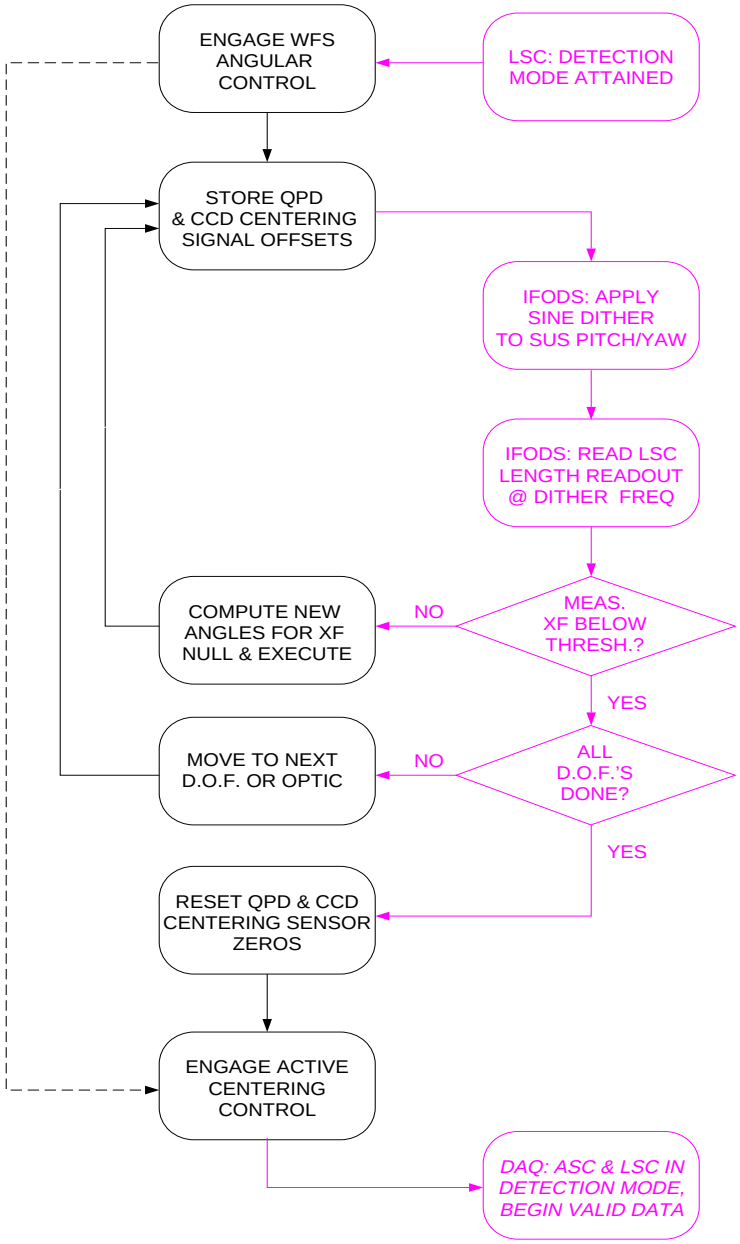

Figure 8 Procedure for determining physical rotation axes of test masses and reconciling centering sensor references. Procedure is only invoked if existing centering references are invalid (e.g., after major optics rework or stack adjustment); dashed path is followed in normal operation.

3.3. Servo Design

The alignment servo must be designed to meet the relevant requirements given in the ASC DRR, which are stated generally as:

- the rms fluctuations of the angles must be held to ≤ 10^{-8} radians (refer to the ASC DRR for a more detailed definition of the angles and the rms requirement for each)
- the servo noise in the GW band must controlled so that it does not degrade the interferometer performance (refer to the ASC DRR for the detailed requirements on the allowed noise levels)

The wavefront sensor noise (in terms of equivalent angle noise) will be larger than the test mass pitch/yaw thermal noise (the shot noise is much larger than the thermal noise - see section 4.3.4. - and the noise may be higher than shot noise at some frequencies of interest); the sensor signals will thus need to be filtered before being applied to the COC optics in order to meet the second requirement. There is a trade-off in the servo design between the front end (sensor) electronics noise and the required above servo-band filtering. The design presented below offers a solution based on a certain assumed level of sensor noise, but there is margin for redistributing this trade-off; this will be further examined as the electronics design advances.

3.3.1. Simplified servo example

The WFS servo is of course a multiple-input multiple-output (MIMO) system - the signals from the individual WFS are combined and filtered (with possibly different compensation for different WFS signals) and then transformed into signals for the individual mirrors. In order to show the feasibility of attaining the above requirements, we present here a simplified single-input, single-output control design.

Figure 19 in Appendix 2 shows a block diagram of the WFS control system which applies generally to the complete MIMO system, but which we apply here to the simplified case. The input θ^{ext} represents the external angle disturbances, which are due to many environmental sources - these inputs come from the model mentioned in section 2.2.1. above, and in Appendix 3 and reference [6] (the local sensor servo is of course not used in this case - see Appendix 3).

The open loop gain, G, for the design example is shown in Figure 9. The loop parameters are given in Table 4. The spectrum of residual angle fluctuations is shown in Figure 10, along with the integrated rms angle as a function of the lower frequency bound for the integration. The ground noise data used in this simulation is the Livingston time series described in Appendix 3.

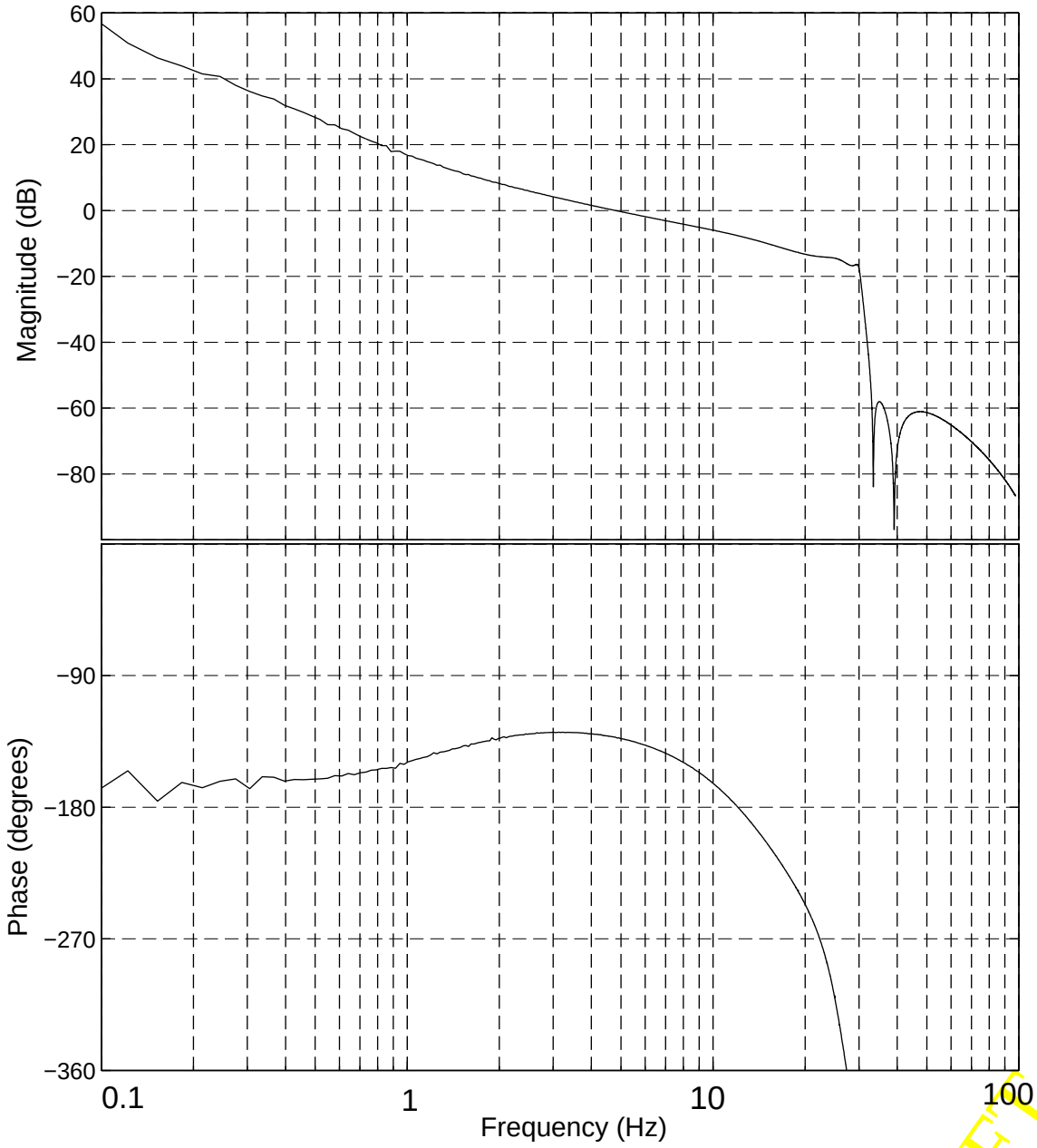

Figure 9 Open loop transfer function of the sample servo design

The residual angle deviation for this simulation is 8.5 nanoradians rms, just below the requirement of 10 nanoradians rms. The angular noise contributed to the mirror above the servo band by the WFS control system is given by the angle-equivalent wavefront sensor noise, multiplied by the open loop gain at the frequency of interest. At best the sensor noise is determined by shot noise. The angle-equivalent shot noise for the sensors is given in Table 7 below; the average angle-equivalent shot noise level is around 10^{-15} rad/√Hz. We will take a more conservative value of 10^{-14} rad/√Hz as the angle-equivalent wavefront sensor (input) noise for this example.

Unity gain frequency	4.5 Hz
(In band) Loop response	2 poles at 0 Hz, 1 zero at 1.5 Hz
High frequency filtering	6th order elliptic, 1 dB passband ripple, 40 dB stopband attenuation
Phase margin	45°
Gain margin	8 dB

Table 4 Parameters of sample servo design

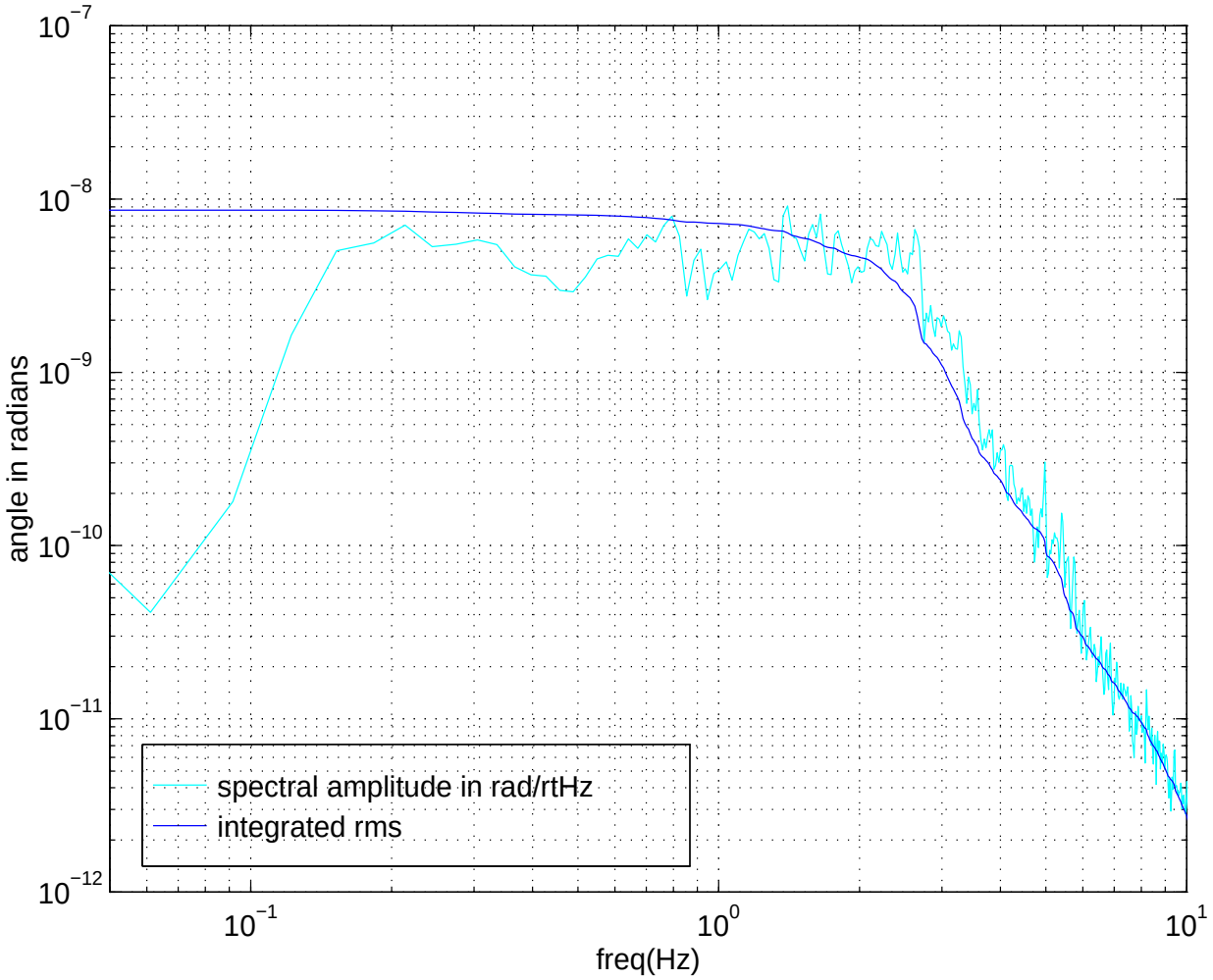

Figure 10 Residual angle fluctuations under WFS servo control. Shown is the spectral density of angle fluctuations, and the rms angle in the band (f-100 Hz).

We have done some exploration of the change in performance when different ground noise inputs and different stack transfer functions are used in the model. Table 5 gives a summary of the results

of this modeling; the same loop transfer function (given in Figure 9) was used in each case (thus the GW band angular noise contribution of the servo is the same as above). In one case - where the HYTEC leaf spring stack is driven by the Livingston ground noise - the residual angle is larger than the requirement; probably a more complicated loop shape - with increased gain at the 1.5 Hz stack resonance - could bring this down below the requirement (probably with some trade-off in the high frequency gain/attenuation).

Ground Noise Input	*Stack Design*	*Residual rms angle*	*Frequency(ies) of dominant fluctuations*
Hanford	HYTEC viton stack	2 nrad	2-3 Hz
Hanford	HYTEC leaf spring stack	4.5 nrad	1.5 Hz
Livingston	HYTEC leaf spring stack	55 nrad	1.5 Hz

Table 5 Results of WFS servo model for alternate ground noise inputs and stack designs.

3.3.2. Comparison with requirements

With the input angular fluctuations predicted by our model, the above servo design meets the residual rms angle fluctuation requirement of 10^{-8} radian for all design cases except for the leaf spring stack driven by (noisy) Livingston ground noise.

The angular noise produced in the GW band also satisfies the requirement (refer to Table 4 of the ASC DRD). Assuming a sensor noise of 10^{-14} rad/√Hz as stated above, the angular noise is below the requirement by a factor of 2 at 40 Hz and a factor of 5 at 100 Hz.

The GW band displacement noise depends on the angle-length cross coupling in the SUS controllers. According to the SYS DRD, reference [1], this cross-coupling is required to be less than or equal to 3×10^{-3} m/rad in the band f = 40 - 150 Hz. At this level of cross-coupling, the ASC-SUS GW band displacement noise requirement is necessarily satisfied if the ASC GW band angle noise requirement is satisfied; we have thus satisfied the displacement noise requirements (by factors slightly larger than for the angle noise).

4. SENSOR DESIGNS

4.1. Sensor Layout

A functional layout of the various ASC sensors is shown in Figure 11, and an equipment location layout for a vertex station is shown in Figure 12. In detection mode the alignment data and the centering data is used by a digital servo to control the mirror angles of the interferometer and the input beam direction (via the beam steering optics). In this mode all other information which is

gathered by the ASC subsystem is for monitoring only. On the other hand, during initial alignment, when no valid alignment data exists, the orientation data provided by the optical levers and the suspension controllers — together with the centering data — is used to align the interferometer to the point where the length degree-of-freedom of the interferometer can be locked.

A table of channel counts and characteristics for the ASC sensors is given in Appendix 4.

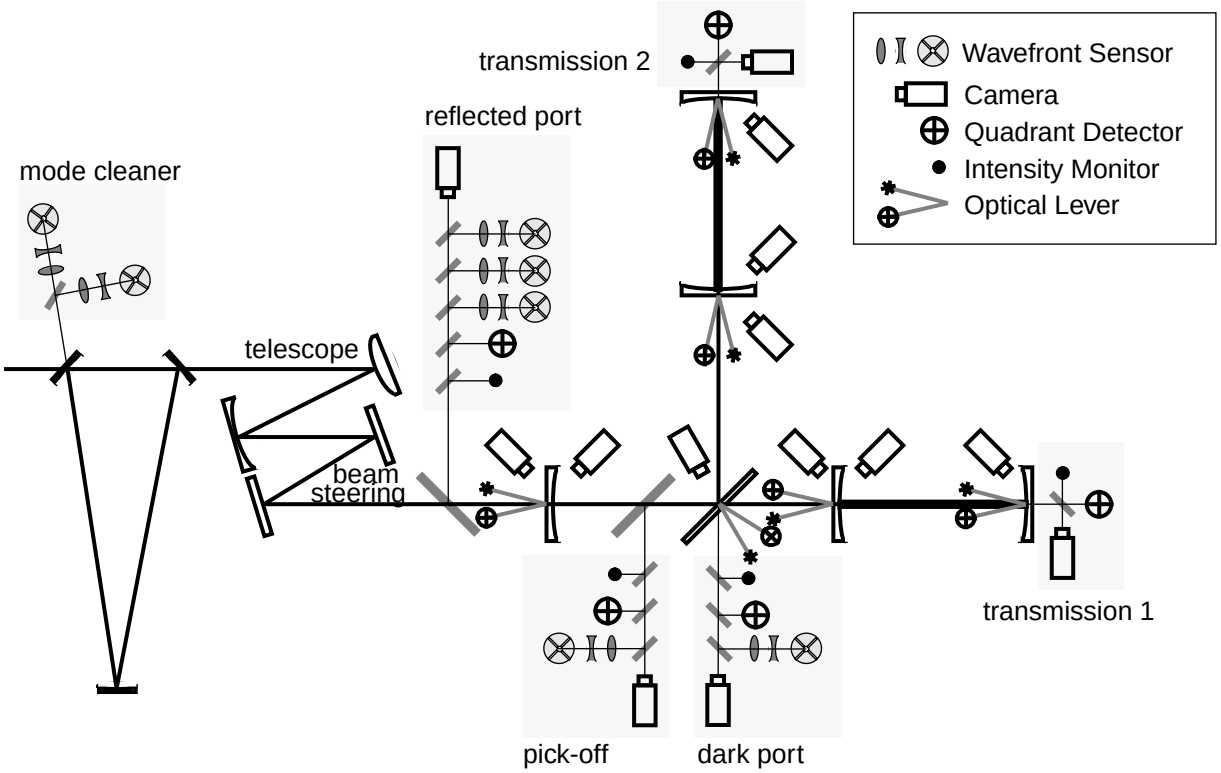

Figure 11 Functional layout of the ASC sensors. The ‘pick-off’ represents a beam from one of the ITM, or the BS, AR surfaces. The ‘symmetric port’ is representative of a sample of the interferometer reflected light.

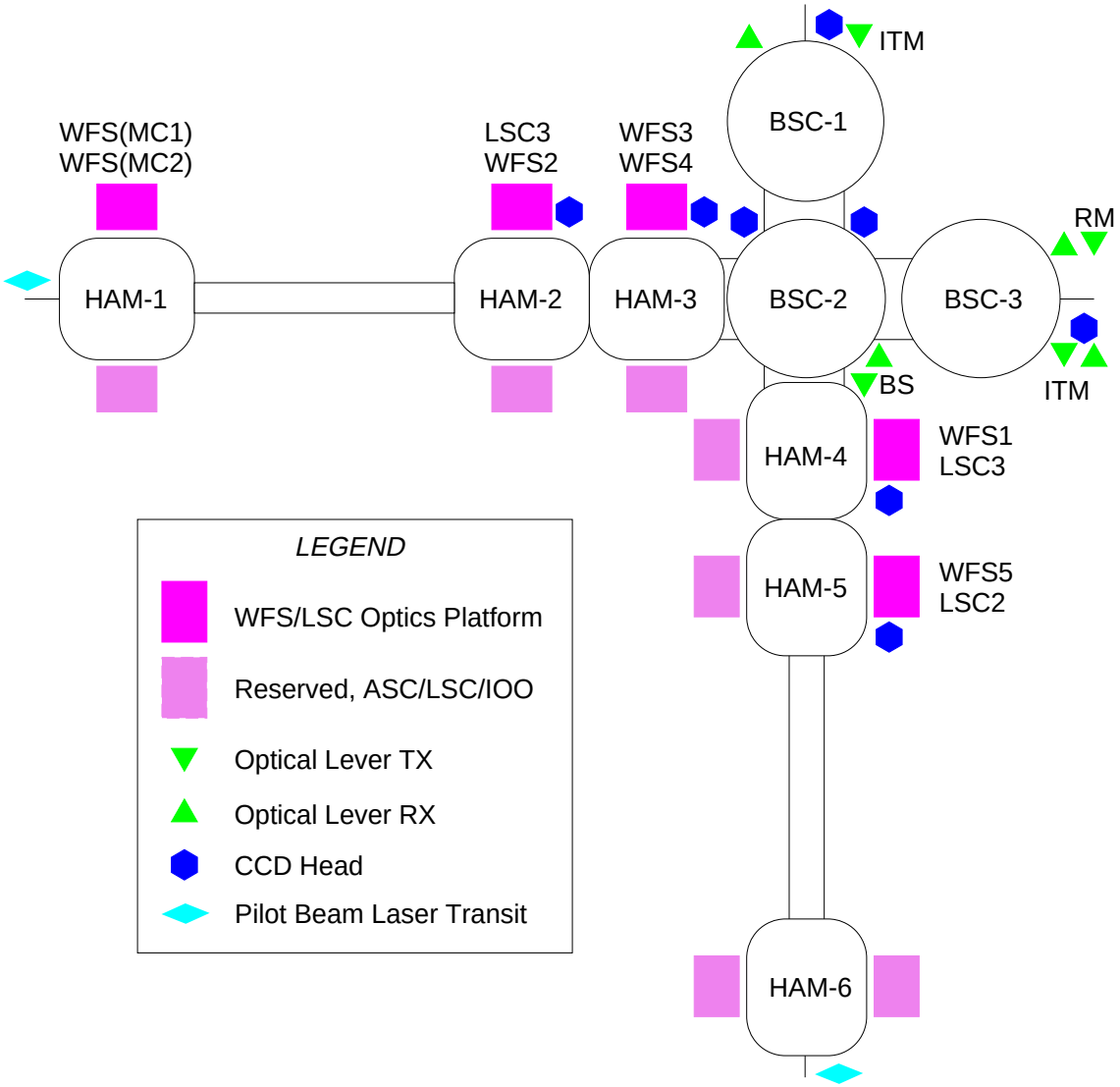

Figure 12 Wavefront sensor, beam centering and optical lever equipment location schematic (vertex interferometer, preliminary).

4.2. Beam Centering Sensors

Figure 13 shows the expected power levels in the interferometer which are relevant for the two types of beam monitors. The scatter loss of 10 ppm is a lower estimate of the total scatter from an optic; for a camera focused on an optic, the power levels in Figure 13 must be multiplied by the fraction of the scattered light that is collected by the camera lens. The essential conclusion is that there is sufficient optical power for the centering sensors described below.

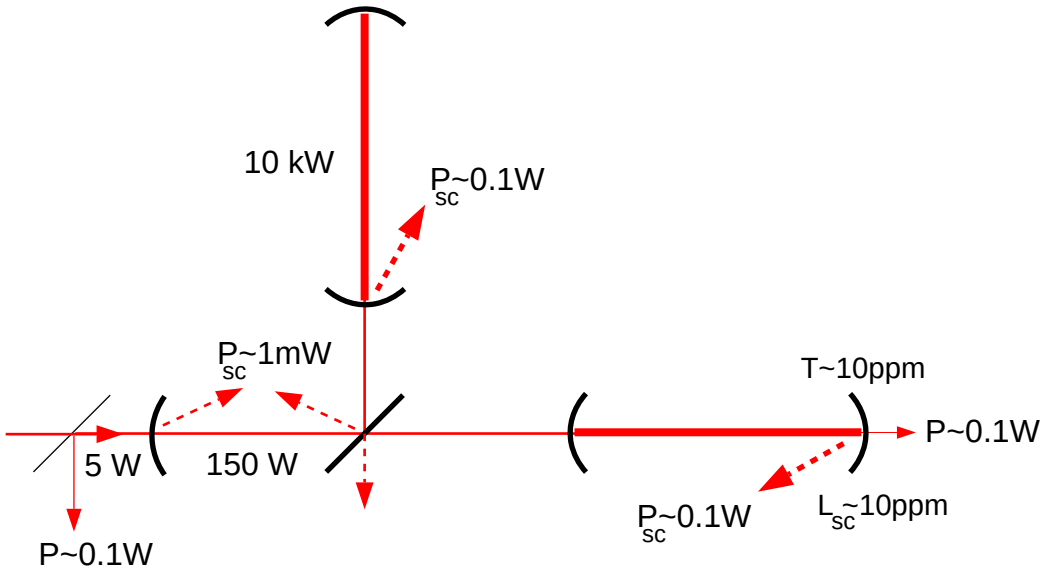

Figure 13 Power levels relevant to the beam position monitors

4.2.1. Quadrant Position Detectors

The beam positions at four ports will be measured with quadrant detectors: the two arm cavity transmissions; the interferometer reflected beam; a sample of the recycling cavity beam (from an ITM or beamsplitter AR surface). These sensors are mounted external to the vacuum on stable mechanical platforms. We expect the position stability of these sensors relative to the suspended optics to be much better than the 1 mm test mass centering requirement over a time scale of at least 1 month (stack drift time scale).

The quadrant detector and associated signal processing are functionally grouped into a Quadrant Monitor Processing Unit (QMPU). The detector signals are digitized locally and sent to the ASC computer (at a modest rate and bit count - see Appendix 4). We may provide the capability for selectable detector transimpedance gains that could compensate for different power levels in the Detection and Initial Alignment modes.

4.2.2. Video Cameras

Video cameras are used to view the vacuum chamber interiors during Initial Alignment, and to monitor the position of the beam on the COC optics; in both cases scattered 1.06 µm light is collected by the camera's lens. The optic's image on the camera will be determined by periodically illuminating the optic with a light source (external to the vacuum).

A camera and associated hardware and processing is grouped into an Image Processing Unit (IPU - see Figure 14). The image from each camera will be processed locally with a standard frame-grabber and some image analysis which returns to the ASC computer various beam parameters,

such as the beam widths and the (*x*,*y*) position of the beam centroid on the camera's image plane. A remotely selectable IR filter is included, as well as remote zoom control on the lens (possibly not for all cameras).

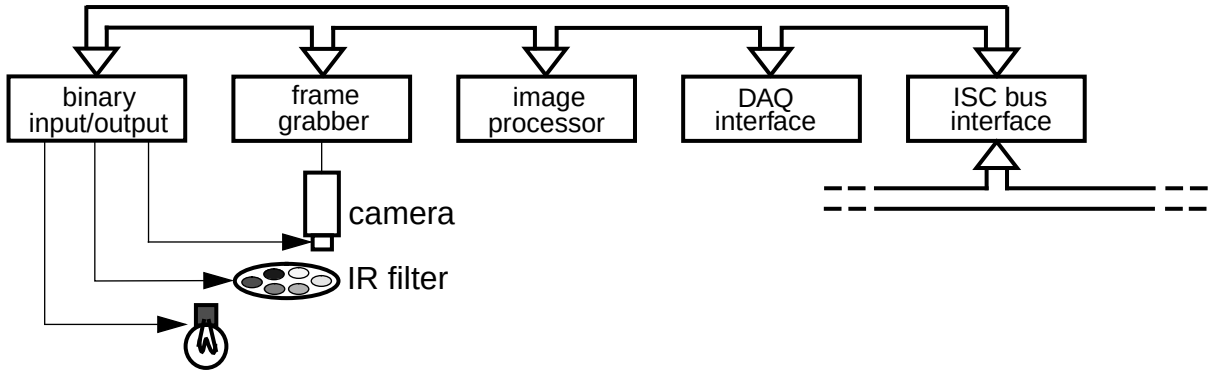

Figure 14 Image Processing Unit (IPU).

4.3. Wavefront Sensors

4.3.1. Number & Location of Sensors

Based on the signal matrix in Table 1 and the comments following it, we have developed a strategy for measuring the five alignment degrees of freedom (ten in two dimensions). Five wavefront sensor heads are included in the design, giving six alignment signals (one head gives two signals, as both I and Q demodulation phases are used). They are as follows:

1. **WFS 1:** At the dark port, at η= 90° and demodulated in Q-phase; measures differential ETM and ITM at a ratio of 2-1.
2. **WFS 2:** At the reflected port, at η= 35° and demodulated at the resonant sideband frequency in:
    a. Q-phase; measures mostly differential ITM.
    b. I-phase; measures common ITM and RM at a ratio of 1-2.
3. **WFS 3:** At the reflected port, at η= 0° and demodulated in I-phase at the **non-resonant** sideband frequency; measures mostly RM
4. **WFS 4:** At the reflected port, at η = 90° and demodulated in I-phase at the **non-resonant** sideband frequency; measures common ETM and ITM at a ratio of 2-1.
5. **WFS 5:** At the recycling cavity port, at η= 35° and demodulated in Q-phase at the resonant sideband frequency; measures mostly differential ITM.

In principle the last sensor (WFS 5) is not necessary — the other sensors give all five degrees-of-freedom. A possible advantage of sensing the field in the recycling cavity (either the recycling cavity or arm reflection port) is that it is less sensitive than the reflected field to the losses in the interferometer. In addition there may be a signal-noise advantage because a large fraction or all of

the one of the AR surface reflections could be directed to a WFS, whereas at the reflected port (where there is more than one WFS) the ASC would be apportioned no more than a few percent of the light. It is included in the design and can be used either to supply a servo error signal or as a diagnostic.

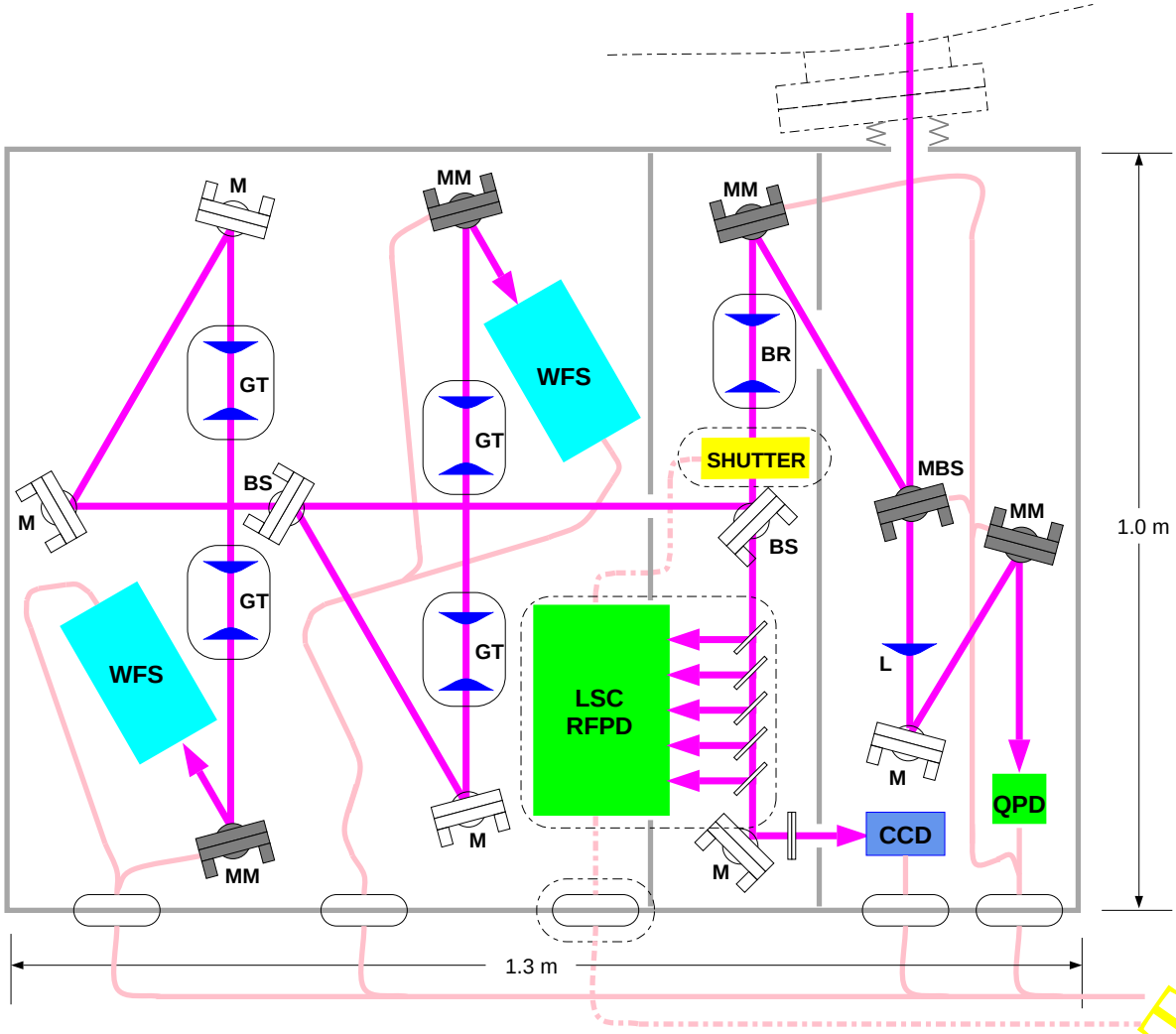

Figure 15 Wavefront sensor head optical bench concept (preliminary). Here M, BS, MM, and MBS are mirrors, beamsplitters, and motorized mirrors and beamsplitters, respectively. GT denotes a Guoy-phase selecting telescope; WFS denotes a wavefront sensor head. LSC components sharing the bench are encircled by dot-dash borders. CCD and QD denote beam centering CCD camera and quadrant photodetector. The assembly is shielded by a light-tight safety/dust/thermal enclosure with internal baffles for scattered light control. Bulkhead connectors are used to pass signal and power wiring through the enclosure. The beam entry path from the vacuum I/O port (top) is shielded by a resilient bellows.

4.3.2. Optical power budget for WFS

The wavefront sensor at the dark port (**WFS 1**) will be apportioned 1% of the dark port light. This is the maximum allowed for preservation of gw-sensitivity (see ASC DRD). The signal that **WFS 1** detects is well aligned with one of the two most sensitive axes for the shot noise sensitivity (the u_2 axis), which is also the axis which has the largest beam jitter sensitivity. Thus a high SNR measurement of this degree-of-freedom is desired, and so the maximum power allotment is taken.

At the reflected port, there are three wavefront sensors. One of these signals (**WFS 2b**) is well aligned with the other most sensitive axis for the shot noise sensitivity (the u_1 axis). The power apportioned to the ASC determines the degradation of the shot noise limited sensitivity of the LSC l_- (Michelson differential) and L_+ (arm common or laser frequency) degrees-of-freedom. We will assume a tolerable degradation of 2.5%, corresponding to apportioning 5% of the reflected light to the ASC. This 5% will be split roughly equally between the three WFS heads.

There are three distinct interferometer beams which sample the recycling cavity field: the beams from the AR surfaces of the two ITMs and the beamsplitter. We apportion one of these beams to the ASC - for definiteness we take it to be an ITM beam. If the ITMs have an AR= 600 ppm the splitting factor for WFS 5 is 0.3.

Modulation Depth of Non-resonant Sideband. The ASC has nominal control over the modulation index of the non-resonant sideband, though there may be some input from LSC if length sensing is done with this frequency. A modulation level which makes a negligible change in the carrier power, and which seems to produce no noise problems for the LSC [4], is $\Gamma = 0.05$. This is the level that will be carried in the design.

The splitting factors and effective optical input power levels for the sensors are shown below.

Wavefront Sensor	*Splitting factor*	*Effective input power, P*	$f(\Gamma)$
WFS 1	0.01	P_{in} = 5 W	0.45
WFS 2	0.01	P_{in} = 5 W	0.45
WFS 3	0.02	$J^2_0(0.5)\cdot P_{in}$ = 4.4 W	0.05
WFS 4	0.02	$J^2_0(0.5)\cdot P_{in}$ = 4.4 W	0.05
WFS 5	0.3	P_{in} = 5 W	0.45

4.3.3. WFS Error Signal Matrix

The matrix of WFS error signals is now determined by the parameters of Table 1, and the sensors and splitting factors defined above. A remaining parameter in Equation (1) is the photodiode factor k^{10}_{PD}. We take a quadrant photodiode, for which k^{10}_{PD} = 0.70; the choice of photodiode geometry

is discussed in section 4.3.5. below. The other remaining parameters in Equation (1) are the demodulator and Guoy phases. In practice neither phase can be set precisely to the desired value. The assumption is made that the demodulator phase can be set to 1° of the desired phase[1], and that the Guoy phase can be set to 5° of the desired phase. The error signal matrix resulting from these choices is shown in Table 6. The entries correspond to the level of rf-optical power per normalized angle; multiplying them by the photodiode responsivity gives the actual rf-photocurrent per normalized angle. Any value which was less than 0.01 of the largest value was set to zero.

M_{ij}	***Angular Degree-of-Freedom***				
Wavefront Sensor	**ΔETM**	**ΔITM**	**$\overline{\text{ETM}}$**	**$\overline{\text{ITM}}$**	**RM**
WFS 1	**-0.33**	**-0.15**	0	0	0
WFS 2a	5.7×10^{-4}	**-0.034**	0	0.0034	-0.0048
WFS 2b	0	0	0	**0.19**	**-0.27**
WFS 3	0	0	-5.8×10^{-4}	-2.6×10^{-4}	$\mathbf{6.1 \times 10^{-3}}$
WFS 4	0	0	$\mathbf{-6.6 \times 10^{-3}}$	$\mathbf{-3.0 \times 10^{-3}}$	5.3×10^{-4}
WFS 5	-5.0×10^{-5}	$\mathbf{-2.9 \times 10^{-3}}$	0	2.9×10^{-4}	-4.0×10^{-4}

Table 6 Matrix of misalignment error signals, with the sensor locations and design parameters given in sections 3.2.1.3 and 4.3.2.. Matrix elements are labelled M_{ij}, where *i* refers to the WFS # (1, 2a, 2b, 3, 4, 5) and *j* refers to the angular d.o.f., in the order shown in the table. Units are Watts per normalized angle**.**

Note that the signals from WFS1 and WFS2b - which are the strongest alignment signals - lie along the directions u_2 and u_1, respectively, as defined in the ASC DRD, Appendix 5. These directions correspond to the most sensitive alignment degrees-of-freedom of the interferometer - u_2 and u_1 being the sensitive d.o.f. for the shot noise sensitivity, and u_2 being the sensitive d.o.f. for beam jitter phase noise.

1. Each WFS signal will be demodulated in I and Q phase; the resulting demodulated signals will be processed in software to extract the appropriate phase. This is how we believe we can achieve this precision.

4.3.4. Noise & Error analysis

Shot Noise

For the aligned interferometer, the shot-noise producing power is due to the TEM_{00} carrier and sideband power at each port, and the higher-order mode power due to mirror distortions (other than tilts).

After demodulation, the shot noise in an alignment signal (signals from opposing quadrants subtracted) is

$$v_{sn} = R_T \sqrt{e \varepsilon \sum_{\mathrm{nm}} (k_{PD}^{\mathrm{nm}} P_{\mathrm{nm}})}$$

where R_T is the transimpedance gain of the photodetector and demodulator, e is the electron charge, ε is the photodiode responsivity, P_{nm} is the power on the photodetector in the (n,m) mode, and k_{PD}^{nm} is the fraction of the (n,m) mode which overlaps the two opposing quadrants of the photodiode.

For a given WFS, the shot-noise in terms of the equivalent angle to which this WFS is sensitive can be written as:[1]

$$\tilde{\mathrm{WFS}}_i^{sn} = \sqrt{\frac{e \sum_{\mathrm{nm}} (k_{PD}^{\mathrm{nm}} P_{\mathrm{nm}})}{\varepsilon \sum_j M_{ij}^2}} \qquad (3)$$

The power levels are estimated using only the TEM_{00} powers calculated by the modal model (for the aligned, resonant interferometer). In this case $k_{PD}^{\mathrm{nm}} = 0.5$; we also take ε = 0.5 A/W. (More accurate would be to use the results of an FFT analysis to determine the power levels and mode distributions at the WFS heads; this will be examined during the preliminary design phase.) With these approximations, the shot noise limited angle sensitivity of the sensors is given in Table 7.

Wavefront Sensor					
WFS 1	WFS 2a	WFS 2b	WFS 3	WFS 4	WFS 5
8.0×10^{-16}	4.9×10^{-15}	5.2×10^{-16}	3.9×10^{-14}	3.3×10^{-14}	3.0×10^{-13}

Table 7 Shot noise limited angle sensitivity of the wavefront sensors. Units are radians/√Hz.

The shot noise clearly does not present a limit to the level of alignment stability achieved in the control band (in fact the light will certainly not be shot-noise limited at control band frequencies).

1. We neglect in this approximation any effects of non-stationary shot noise.

In the gw band, however, the shot noise angle is much larger than the pitch/yaw thermal noise of a test mass - the SUS requirement on pitch/yaw thermal noise is $< 5\times10^{-18}$ rad/$\sqrt{\text{Hz}}$ at 100 Hz. The control signals from the WFS will thus have to be well filtered before being applied to the test masses.

Sources of Alignment Errors

Clearly the angle measurement at low frequency will be limited not by shot noise but by other sources such as electronic noise and offsets, and optical errors. Estimates of the errors in the detection angle due to some such sources have been made and are shown in Table 8. Not yet analyzed are errors due to the existence of higher order optical modes (m+n >1) in the system, due to the imperfect optical surfaces. These will be analyzed during the preliminary design phase, using the output of an FFT analysis to determine the higher order mode content at the detection ports.

Error	*Estimate of magnitude*	*CMRR (dB)*	*Resulting Angle Error (radians), WFS #*				
			1	*2a*	*2b*	*3*	*4*
Residual length deviations (in meters)	$L_- = 10^{-12}$ $l_- = 10^{-10}$	30	6×10^{-11}	5×10^{-11}			
	$L_+ = 4\times10^{-12}$ $l_+ = 4\times10^{-10}$	30			2.2×10^{-10}	3×10^{-9}	2×10^{-9}
RF pickup (per segment)	< 1 μamp	20	$<5\times10^{-12}$	$<7\times10^{-11}$	$<5\times10^{-11}$	$<4\times10^{-10}$	$<3\times10^{-10}$
Demodulator offset (with $R_T = 5$ kΩ)[a]	<10 mV	0	$<1\times10^{-11}$	$<2\times10^{-11}$	$<1\times10^{-11}$	$<8\times10^{-10}$	$<6\times10^{-10}$

Table 8 Estimates of detection errors in terms of equivalent mirror angle.

a. R_T is the transimpendance gain of the WFS head up to the demodulator output. The value used here serves as an example to show that demodulator offset is not expected to be a problem; the actual transimpedance gain depends on dynamic range and noise issues, and will be determined as the electronics design advances. For reference, the value in the current WFS heads is of order 1 mega-ohm [7].

4.3.5. Wavefront Processing Unit

A block diagram of a wavefront processing unit is shown in Figure 16. The unit includes: the sensor head and Guoy phase telescope, with motorized mirror mount for remote beam centering; the

demodulators for the rf-signals; ADCs for the dc and demodulated-rf signals; a signal processing unit; state control outputs and status inputs.

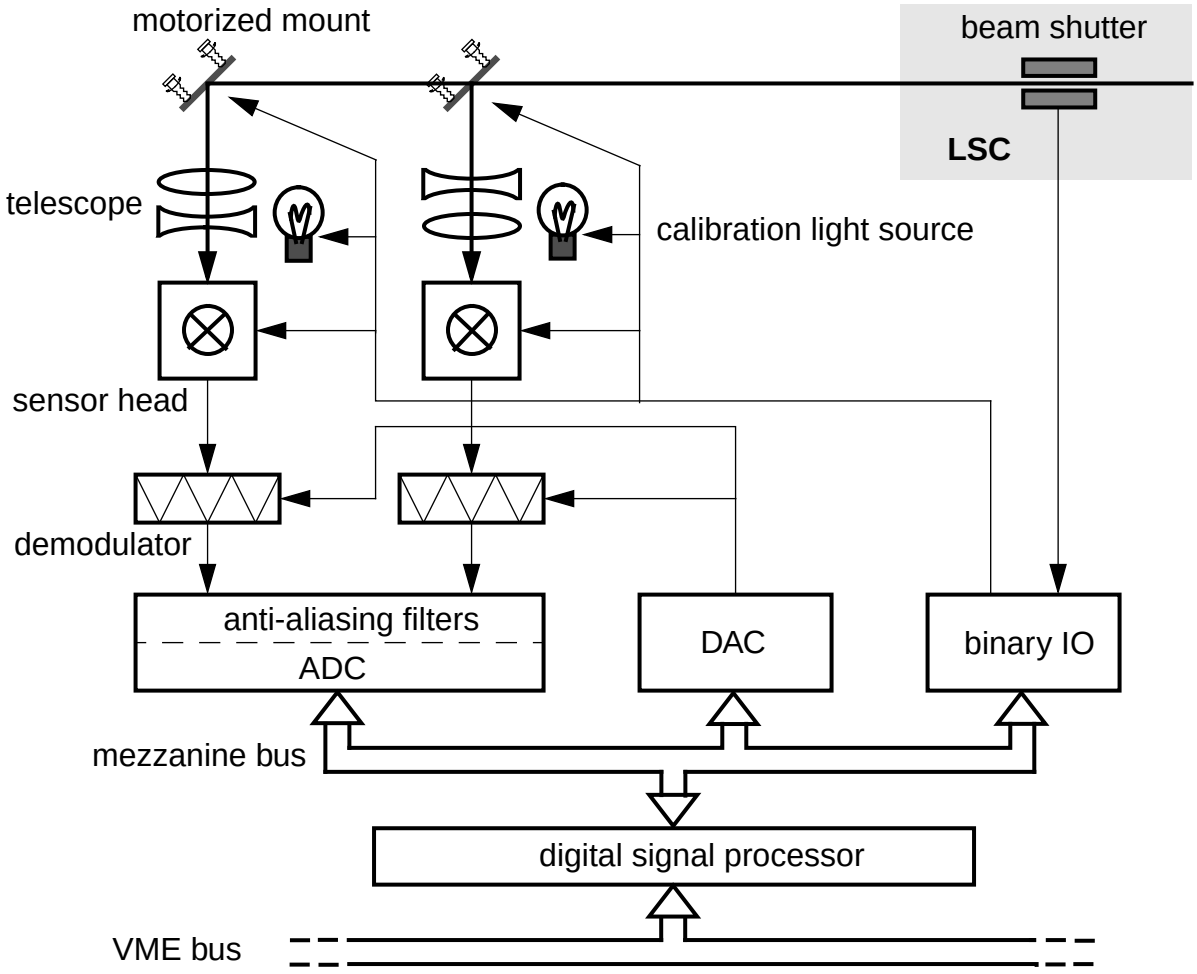

Figure 16 Wavefront Processing Unit (WPU) - more than one sensor head (and associated telescope, demodulator, etc.) may be interfaced to one ADC/signal processing unit. The motorized mirrors are for remote beam centering. The beam shutter sends a status indication to the WPU.

4.3.5.1 Sensor head

The design of the wavefront sensor head and demodulation electronics will be based as much as possible on the prototype wavefront sensors that have been developed for the FMI (Fixed Mass Interferometer) Alignment experiment. This hardware is described in detail in reference [7].

One design choice is the shape of the multi-element photodiode. Prototype sensors have used quadrant photodiodes, both with and without a hole in the middle. The existence of the hole offers the possibility of including a fifth photodiode behind the hole, allowing one to detect even order

modes due to mode mismatch. We choose for our design a quadrant photodiode without a hole, because this geometry is more tolerant to the beam size on the diode, and has essentially the same S/N (due to shot noise) as does the photodiode with hole [7]. In addition we feel it is a practical advantage to decouple the mode-matching monitoring from the alignment detection.

The photodiode will most likely be of silicon, enhanced for near-infrared response, such as the Centronic Inc. model QD50-4X quadrant (responsivity of $\varepsilon = 0.5$ A/W at 1064 nm).

4.3.5.2 Guoy Phase Telescopes

The telescopes which control the Guoy phase between the TEM_{00} and $TEM_{10/01}$ modes are considered part of the WFS heads, and will be made of standard commercial lenses. For a given WFS, the Guoy phase will be set to provide the maximum sensitivity for the degree-of-freedom that the WFS is intended to detect (e.g. the Guoy phase for WFS 1 will be set to $\eta = 90°$). A possible exception is WFS 2, where one might choose to operate slightly away from the Guoy phase which gives maximum sensitivity ($\eta = 35°$) in exchange for further reducing the sensitivity of the WFS 2b signal to $\overline{\theta_{ETM}}$.

We expect it to be possible to adjust the Guoy phase to within 5° of the desired phase. The telescope lenses for a given WFS will be mounted on a rail, and the lens separations will be adjusted off-line. No remote positioning of the telescope optics is planned for.

4.3.5.3 Signal Processing

The demodulator outputs will be over-sampled to decrease the level of digitization noise. As shown in Figure 16, a single digital signal processor may serve more than one WFS head. The front-end processing includes for example: individual channel gain corrections; differencing of opposing quadrants; offset corrections; vertical-horizontal separation. The output of the front-end processing is intended to be (in some units) the ten angles in the interferometer (ALIGNMENT DATA). The signal count and characteristics of the WPU are given in Appendix 4.

4.4. Optical Lever Design

The optical lever system used is a relatively simplified, short-arm “local” system. With target stability at the 0.01 mrad level, the complications of long (> 2 m) baselines and fiducial monitoring appear unnecessary.

The system employs a 3 mW-class multimode visible laser diode source, coupled by singlemode, polarization preserving fiber to a projection optics package. This is mounted to the facility foundation near a vacuum I/O port with a view of the suspended optic to be monitored. The projection optics package contains a connectorized fiber collimator and beam expander. A remote-controlled kinematic steering mirror directs the expanded output beam (radius $w \sim 3$ mm, power $P \sim 1$ mW) into the vacuum I/O port. Assuming a direct line-of-sight to the suspended optic is available (TBD) the beam is reflected to a symmetrically placed I/O port and leaves the vacuum chamber.

A second remote-controlled kinematic steering mirror collects the beam and directs it onto a quadrant photodetector, which detects four analog photocurrents. These are processed by the control electronics to provide pitch, yaw and total detected power output signals. The system may be calibrated by controlled test motion of the final kinematic steering mirror.

In the event a “mirror-image” beam I/O port is not available to pass the output beam, a relay periscope device just inside the vacuum wall will be used to translate the beam to the nearest port (Figure 17). Similar in principle to the Periscope Tool described above, but vacuum-compatible and with relaxed parallelism and stability specifications, this unit will be mounted to the I/O port itself. A true periscope arrangement is preferred to minimize the influence of chamber motion on the readout. Applications of this device and detailed specifications are TBD pending detailed optical layout.

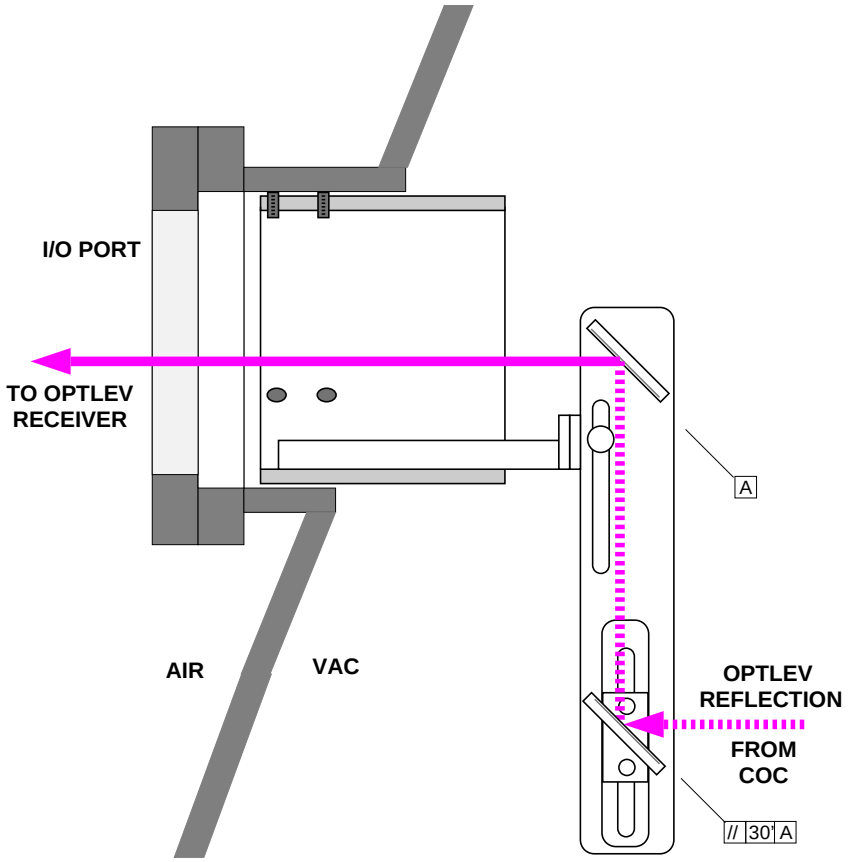

Figure 17 Optical lever output translation periscope. Units will permit recovery of optical lever output beams falling within approximately 50 cm of nearest I/O port, and are field-installable through nozzle with port cover removed. Incidence and specifications TBD pending detailed optical beam layout.

The optical lever transmitter and receiver are relied on to maintain an optical direction reference through service or maintenance intervals; however, in some applications they will need to be dismantled to allow cover removal and internal access to the vacuum envelope. The mounting pedestals will therefore be kinematically mated to semi-permanent baseplates anchored to the LVEA/ VEA floor slab (Figure 18). Repeatability of better than 0.1 mrad in all relevant axes will be achieved.

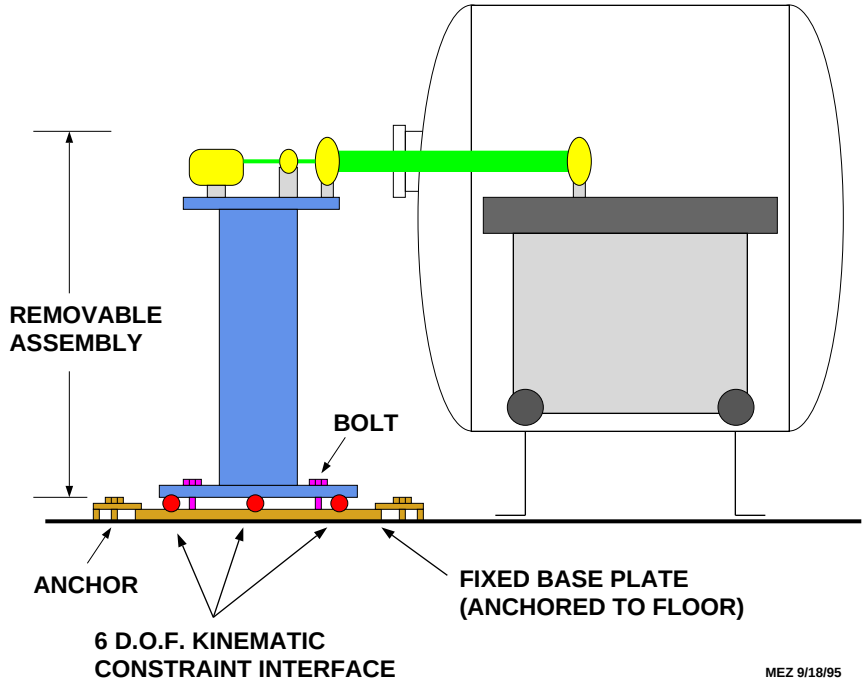

Figure 18 Demountable optical lever Tx and Rx support scheme.

5. DIAGNOSTICS

5.1. Alternate ASC control sensing

For diagnosis and commissioning of the wavefront sensing system itself, and for various diagnostic tests of other subsystems, ASC will provide means for interferometer operation using independent alignment inputs from the local suspension sensors or from the optical levers. Some combined modes (in which subsets of the optical system are controlled by different sensing paths) may also be provided to enable clean separation of variables, for example in diagonalizing control matrices.

While interferometer sensitivity may be directly degraded, it is expected that deleterious alignment errors will appear over several-minute timescales as auxiliary alignment references drift

with respect to the ideal cavity axes. It should thus be possible to directly check for noise induced by the wavefront system itself at near-optimal sensitivity, by using the auxiliary sensors in a “fly-wheel” mode.

5.2. Support for nonstandard optical configurations

For commissioning and diagnostics, as well as for initial alignment (see Section 2), it will be necessary to support operation of nonstandard optical configurations. Some of these diagnostic configurations are detailed in the LSC Conceptual Design, LIGO T960027. At this time it is not guaranteed that proper operation of the wavefront sensing alignment system in all of these modes is possible without significantly increasing the design’s complexity (in some cases, additional modulation capabilities might even be required from LSC and IOO). Still, it is worth noting that the extremely tight alignment enabled by the wavefront sensing system may not be required in most such modes, which have lower ultimate sensitivities by definition. As a result, local sensor or optical lever control (above) can also support these operations.

It is advantageous (though not critical) to use wavefront sensing to automatically maintain optimum alignment of the short-arm recycled Michelson during the iterative initial alignment procedure described in Section 2; at present it appears feasible to accommodate this particular configuration by changing WFS system loop gain and demodulation phase to compensate the loss of sideband resonance in the recycling cavity.

5.3. Mode Matching

ASC hardware and software will support determination of the overall modal overlap between the incident beam and the interferometer optics, as well as the mismatch between the two arm cavity modes. While the WFS concept is extensible to interrogation of generic wavefront mismatches in addition to tilts and translations, this would require increased complexity, an increased number of RF detection channels, and a new line of development and prototyping. The advantage, a real-time picture of the wavefront mismatch, is unlikely to be necessary until and unless mirror heating or other effects cause appreciable mode changes on dynamical timescales (not expected at initial circulating power levels).

As a result, we will provide a simplified quasi-static readout of the mode matching, useful for fine-tuning telescope adjustments or diagnosing errors. The intensity picture of the light from the symmetric and antisymmetric ports, as monitored by four beam centering CCD cameras while the interferometer is in operation, will be digitized and fit to expansions of radial modes (with a sign ambiguity, which we will address shortly). In normal operation, the action of the wavefront sensing alignment control system will drive the lowest odd-order mode amplitudes to a minimum. Amplitudes of higher (even-order) modes in the fit will correspond to the degree of mismatch between the wavefront curvatures and waist diameters. Placement of two of the CCD cameras behind Guoy-phase propagating telescopes will allow separate determination of waist size and

position (or curvature) errors for each readout, by giving equivalent “near field” and “far field” patterns.

To resolve the sign ambiguity (e.g., “which beam is too large, the cavity mode or the input?”) we can invoke the following procedures:

- Disable interference (grossly misalign ETM, for example) and accurately measure absolute mode size of input beam; compare with premeasured core optic curvatures and measurement of transmitted cavity mode.
- Deliberately misalign the input couplers, beamsplitter or recycling mirror by a known angular increment and observe the correlated motion of the intensity pattern.
- Change the IOO telescope setting by a known increment and recheck the intensity pattern.

The first method is probably only accurate enough for relatively gross mismatches; the second method is most applicable to determining differential errors between the arm cavities, and the last method is expected to be used iteratively to make the final adjustments to the IOO telescope during commissioning.

5.4. WFS calibration

We will have the capability of testing the WFS heads in-situ with calibration light sources, as shown in Figure 16. These serve to verify the basic functioning of the heads, and to calibrate the amps-to-volts conversion of the units.

The matrix of mirror angles and WFS signals will be determined by a dithering routine similar to that described in section 3.2.2.2 (it may in fact be a subset of this routine). The measurement will likely be made with the WFS system loops engaged, using angle modulation frequencies that are above the loop unity gain frequencies.

6. OPEN ISSUES

6.1. Sensors for maintaining acquisition alignment

Either the optical levers or the suspension sensors can be used to control the angles of the mirrors in the Initial Alignment mode (during the transition to Acquisition Alignment) and the Acquisition Alignment mode. At this point in the design and modeling efforts, it is not clear which, if either, of the two presents an advantage. This will be further examined as the optical lever and suspension sensor designs progress, and as the relevant factors in the modeling are refined. In any case, the control system will be designed with the option of using either sensor during these modes of operation.

6.2. Frequency response of WFS signals

In the design of the sample Detection mode control loop in section 3.3.1., the assumption was made that the WFS error signal was independent of the frequency of the mirror angle modulation(s), at least up to ~50 Hz. To date the modal model calculations have assumed static misalignments, but modeling efforts currently underway will include dynamic misalignments; by the time of the ASC PDR, the effects of dynamic small angle misalignments will have been made and will be incorporated into the modeling.

The expectation is that the WFS signals will be independent of frequency in the band of interest. This is because the only instance where the $TEM_{10/01}$ mode is resonant is in the recycling cavity for the sidebands, and this resonance has a width of ~ 100 kHz. The $TEM_{10/01}$ mode does not experience the resonance of the arm cavity, nor of course of the double cavity. The $TEM_{10/01}$ modes which are produced in the interferometer thus propagate to the detection points without any frequency dependence.

6.3. Acquisition alignment

The procedure for attaining the Acquisition Alignment mode described in section 2.2. has not been fully developed, and in fact is not necessarily the procedure we will adopt. A major unknown issue at this time is the operation of the LSC locking system in the presence of misalignments (i.e., the acquisition alignment tolerance). This is the subject of current modeling efforts, and it is expected that this modeling will guide us in further developing the procedure for attaining acquisition alignment. We think it likely that we will converge on a combined LSC & ASC lock acquisition algorithm, and the ASC design will be advanced keeping this capability. Since the interferometer lock acquisition procedure is infrequent, we do not need an ‘optimum’ procedure, just one that will work in a reasonable time span.

APPENDIX 1 DEFINITIONS AND PARAMETERS

The interferometer parameters used for the calculations in this document are listed in Table 9. Any differences from the baseline interferometer design will be incorporated for the preliminary design. The definitions for mirror angle degrees-of-freedom are given in the ASC DRD, section 2.4.

Parameter	Unit	arm (ITM)	arm (ETM)	recycl. (RM)	BS
length (common / differential)	m		4002.5	7.5 / 0.14	
power transmission	%	3	0	4	0.49995
losses	ppm	100	100	100	100
radius of curvature	m	–14540	7400	–9851	∞
modulation frequencies	MHz		resonant	30.0	
			non-resonant	20.0	
modulation depths	Γ		0.5	0.05	
wave length	μm			1.064	

Table 9 Interferometer parameters used in the modeling.

APPENDIX 2 WFS CONTROL BLOCK DIAGRAM

For evaluating the effects of noise and other errors in the wavefront sensor system, the block diagram of this control system is shown in Figure 19.

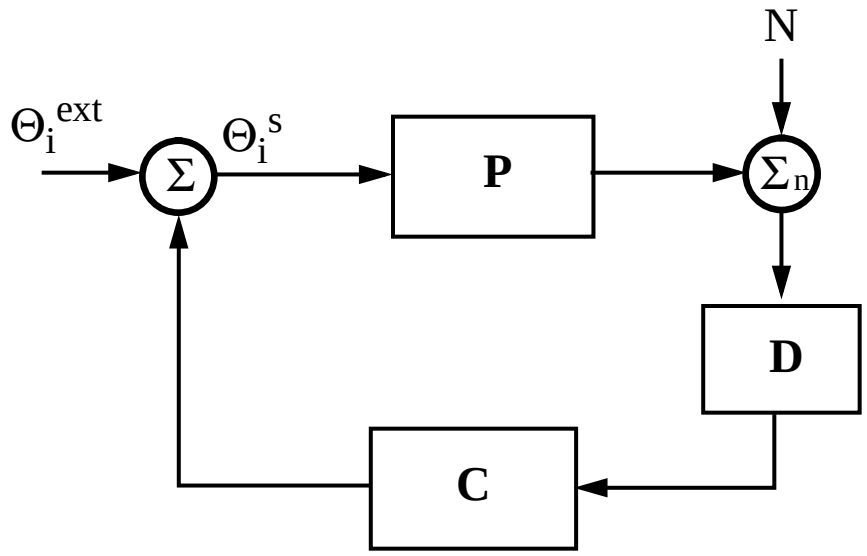

Figure 19 Control block diagram of the WFS servo system

The plant matrix **P** represents the conversion from mirror angles to photocurrent in the wavefront sensor. The action of the demodulator is represented by **D**. The servo controller matrix **C** represents the transformation of the demodulator signals to applied mirror angle correction (including all loop filtering). The (normalized) input angle fluctuations are Θ_i^{ext} and the servo corrected mirror angles are Θ_i^{s}. Various types of noise and error terms can be added at the summing junction

Σ_n, including shot noise, electronics noise, offsets due to optical and electronic origin, etc. The open loop gain of the complete loop is represented by **G = CDP**.

The mirror angles are affected by a noise term through the loop equation:

$$\Theta^s = \frac{\boldsymbol{C} \cdot \boldsymbol{D}}{1 + \boldsymbol{G}} \cdot \boldsymbol{N}$$

There are two interesting regions of loop gain:

1. High gain. The error in the controlled angle due to a particular noise source is determined by the inverse of the plant matrix:

$$\Theta^s = \boldsymbol{P}^{-1} \cdot \boldsymbol{N}$$

2. Above the control band. The angular noise produced above the control band (in the gw band) by the loop is given by:

$$\Theta^s = \boldsymbol{CD} \cdot \boldsymbol{N} = \boldsymbol{GP}^{-1} \cdot \boldsymbol{N}$$

APPENDIX 3 MODEL FOR ANGULAR FLUCTUATIONS

Figure 20 shows the flow diagram for pitch angular noise. The coordinate system has its origin at the "rest position" of the mirror's center of mass, the vertical axis being the "*y*" axis pointing up in the direction of local gravity, and the "*z*" axis pointing along the optical axis. (The coordinate system convention follows the one described in **LIGO-T952007-02**, ASC DRD, section 2.4).

Since the mirrors are curved, a horizontal light beam reflected above or below the center in the mirror will have a tilted return path. Thus, vertical motion of the mirror will be seen as pitch angular noise. This vertical-to-pitch coupling (which adds to the observed angular noise, but is not a physical angular motion of the mirror) is shown at the left of the diagram in Figure 20, with the last coupling being $y_t / R_m \rightarrow \Theta_{mirror}$.

At the very bottom of Figure 20, we have the ground motion: we will need to know vertical (y_g)and horizontal (z_g) displacements, as well as ground tilts (θ_g). The building foundations will transfer the ground motion with some transfer functions, and will add its own response to thermal and acoustic excitations, producing some net displacement and tilt of the building floor, y_f, z_f, θ_f. The seismic isolation stacks sit on this floor, and transmit the floor motion with (well designed, non trivial!) transfer functions. They will have cross couplings (that we neglected in the building foundations transfer functions): for example, variations in the spring properties will couple verti-

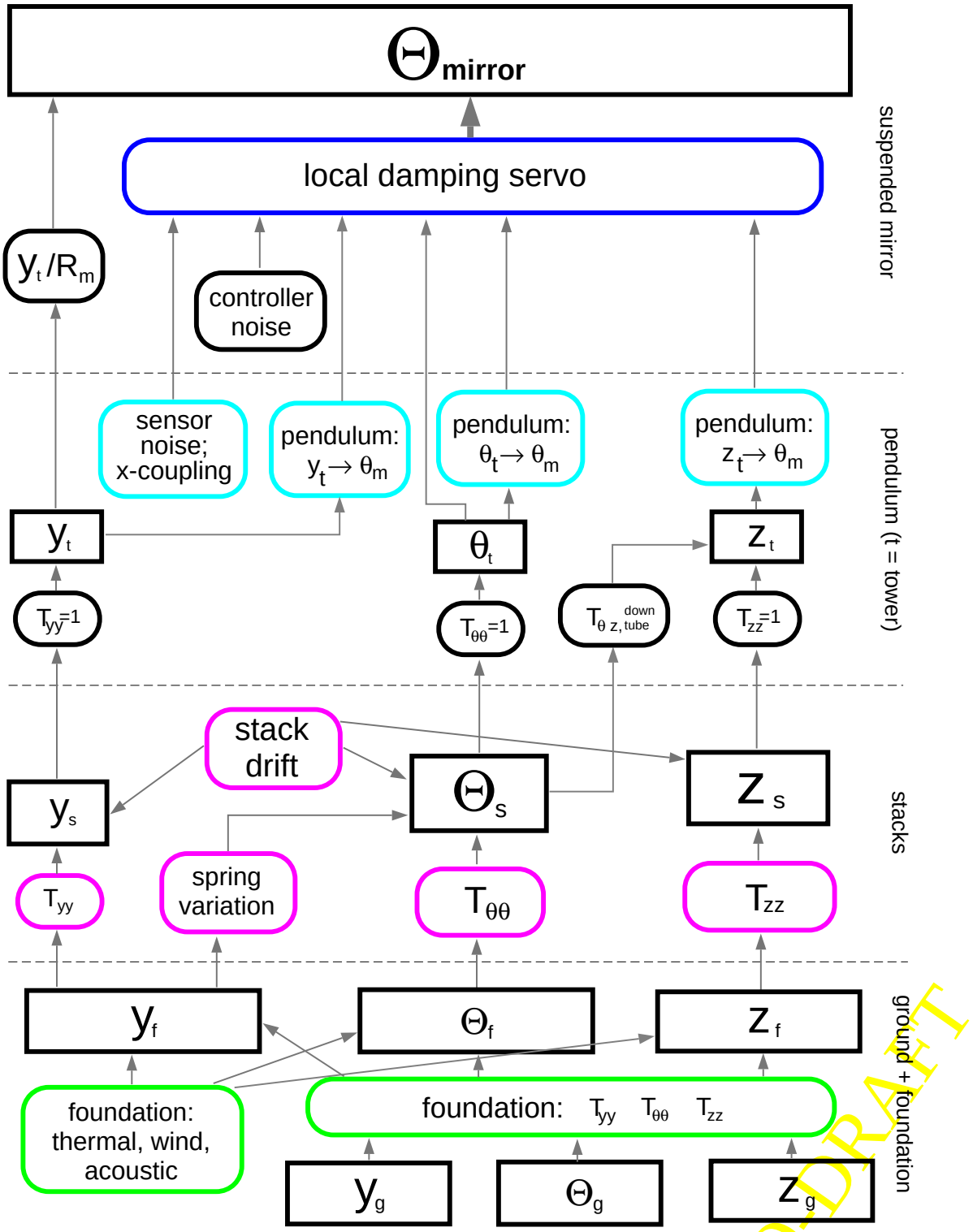

Figure 20 Flow diagram showing the sources of environmental noise converted into angular (pitch) noise of the mirror suspension.

cal motion to pitch and horizontal motion to yaw. The stacks will also “drift” in position and orientation.

The suspension towers will sit (or “hang”) from the last stack stage, and although in principle they have mechanical resonances, we will consider those transfer functions to be unity at the frequencies of (our) interest. What we actually need is the motion of the suspension points: the angles will essentially be the angular motion of the stack optics plate, but the displacement of the suspension points will depend on the position of the suspension tower with respect to the stacks. In the BSC, for example, where the suspension tower is attached to a 1-m long “downtube”, a pitch angle of the stacks will cause a displacement of the suspension tower. If the tower is not at the center of the optical table, stack angles will also couple into suspension tower displacements. (The former coupling is included in the model, the latter is not).

The tower motion excites the pendulum pitch in several ways. Some of these couplings and others were described by S. Kawamura in reference [8]. The horizontal motion of the suspension points excites both the horizontal and the pitch motion of the mirror (as in a classical “physical pendulum”): This is the $z_t \rightarrow \theta_m$ box. If we take into account the wire elasticity, the angular motion of the tower also excites the pendulum pitch, bending the wires at the top: this is the $\theta_t \rightarrow \theta_m$ coupling. If there is an initial imbalance in the mirror balancing, and the line between the wires’ attachment points does not go through the mirror center of mass, a vertical motion of the tower will produce a torque and excite the pitch motion: this is $y_t \rightarrow \theta_m$.

All the resonances except the vertical one are damped with the local controllers. The local sensors used in the controllers are attached to the tower, so they sense the difference between pendulum motion and tower motion. The tower motion thus couples into the pendulum motion also through the servos. Furthermore, the electronic noise in the sensing and driving will couple into the pendulum motion, as well as imperfect orthogonality of the sensing/driving matrix. The “local damping servo” box then couples its inputs, tower motion, into pendulum motion both mechanically and electronically, and adds its own noise sources.

In the model used for the Detection mode servo control, the local damping was replaced by a loop using a WFS for the angle detection. This servo has only the mirror angle and its own sensor noise as inputs (i.e., its input does not depend on the suspension tower tilts). The results presented in section 3.3.1. used the WFS servo for pitch control, and the local damping servo for longitudinal control.

MATLAB Model

Once we provide each transfer function and noise generator mechanism in the block diagram, we can predict the final mirror motion spectrum. However, when the mechanisms have so many different time scales, it is also very instructive to have a “time domain” model of the system. We were able to do this with the SIMULINK toolboxes in MATLAB, where we modeled each input noise with a random time series with the appropriate spectrum (or an actual time series in the case

of ground noise), and we created a zero-pole function for each transfer function. Details of the model can be found in reference [6].

For convenience, the model is separated in two “blocks”, one involving the transformation of ground noise into motion of the stack optics plate, and another converting the optics plate motion into mirror motion. The first block, involving ground+building foundations+stacks, is shown in Figure 21.

The blocks used in the coupling from the stacks to the pendulum are based in the ones used by S. Kawamura in ref. [8]. Each shaded box in the block diagram represents a vector that is stored in workspace, in particular the main outputs of this block are *stck_tilt* and *stck_disp* (stacks tilt and displacement, respectively).

At the ground level, we input time series (or vectors) (t, y_g, z_g) that represent the ground noise. To get the ground tilt, we use the vertical spectrum filtered by a transfer function, obtained assuming that if the ground is moving vertically at a frequency ω with an amplitude $x(\omega)$, with a wave number function $k(\omega)$, then the tilt is going to be $k(\omega)x(\omega)$.

The data used for ground noise are time traces taken by A. Rohay at the sites with a seismometer CMG-40T. The data sets are 10 minutes long, taken at the Livingston site on Day 303 Hour 19 (Greenwich mean time), and on Day 345 Hour 04 at the Hanford site. Each set was taken at the site of the corner station, and each set covers the ‘noisiest’ stretch of data in the complete data sets for each site. We have taken as “horizontal” in both sites the “north” direction, which is parallel to the South Arm of the LIGO site at both Livingston and Hanford.

The floor motion is transmitted through the building foundations and then through the stacks. The stacks have some horizontal-to-horizontal and tilt-to-tilt transfer functions, with a shape depending on the springs used (viton, coil or arch (leaf) springs are the ones considered and modeled by Hytec). We have used both viton and leaf spring stacks to study the residual pitch angle; the transfer functions for each were supplied by Hytec.

The second “block” used in the modeling, with the coupling between stacks and pendulum motion, is shown in Figure 22. It uses as inputs the output vectors of the previous block, *stck_disp* and *stck_tilt*, and it provides as outputs (among other vectors) time traces for the pendulum displacement z and pitch angle θ.

Pitch Controllers

Three different controllers were used between the angle sensor (local sensor or WFS) and the pitch torque input - two for the local sensing and one for the WFS. These controllers are (see Figure 23):

1. Local sensing/velocity damping: standard velocity damping with quasi-critical damping; exact model can be found in reference [8].

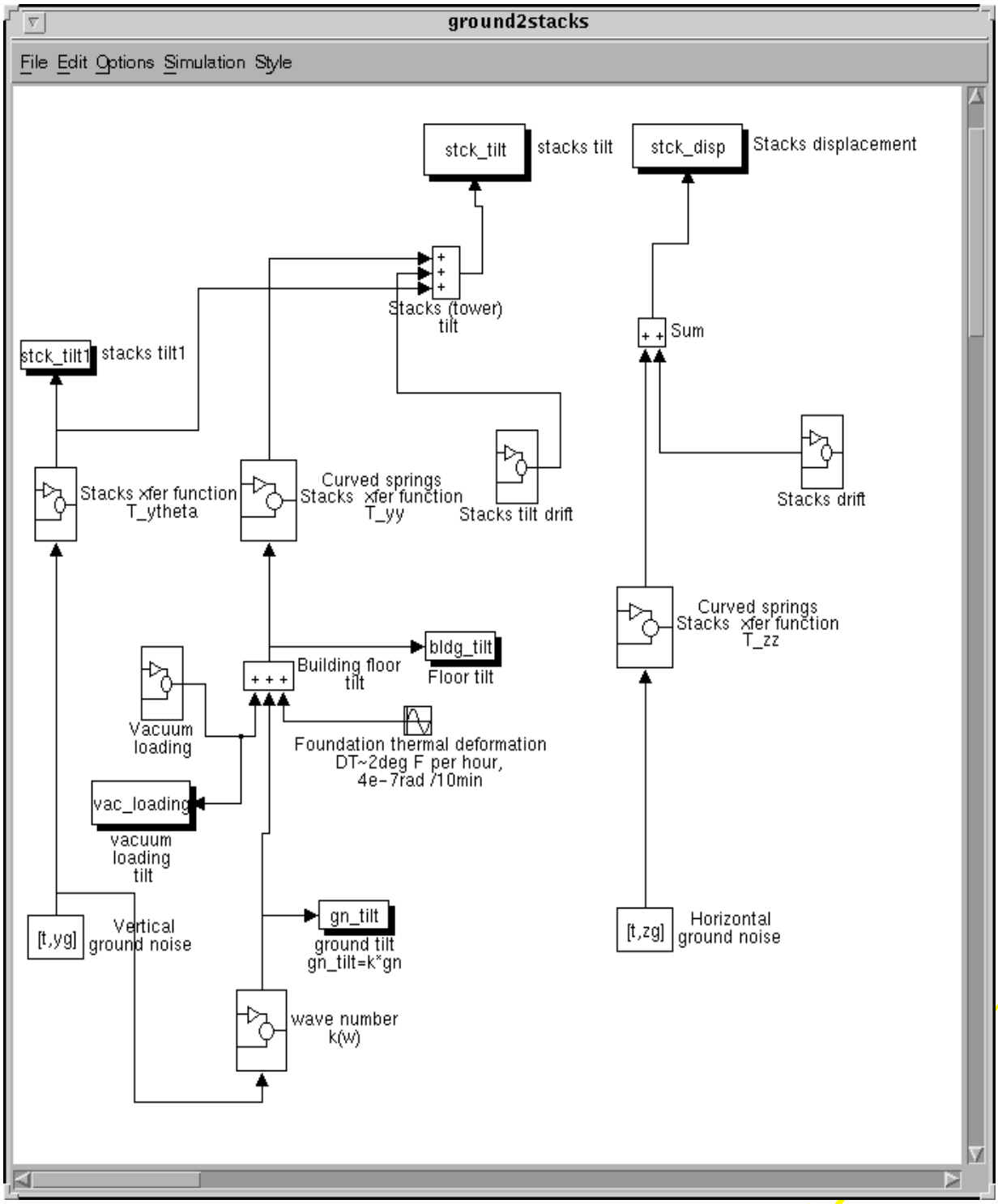

Figure 21 Block diagram for the evolution of ground motion into stack motion.

2. Local sensing/modified feedback: velocity damping with a parallel restricted bandwidth gain path, providing gain at the micro-seismic peak frequency of 0.15 Hz
3. WFS/detection mode servo: loop response as described in section 3.3.1.

In each case the appropriate sensor noise was added to the loop. In the modified local feedback model, the multi-pole low-pass filters which traditionally precede the coil drivers have been removed. This leads to a better phase margin and somewhat smaller rms angle fluctuation - possibly useful for the Acquisition Alignment mode when GW band noise is much less important.

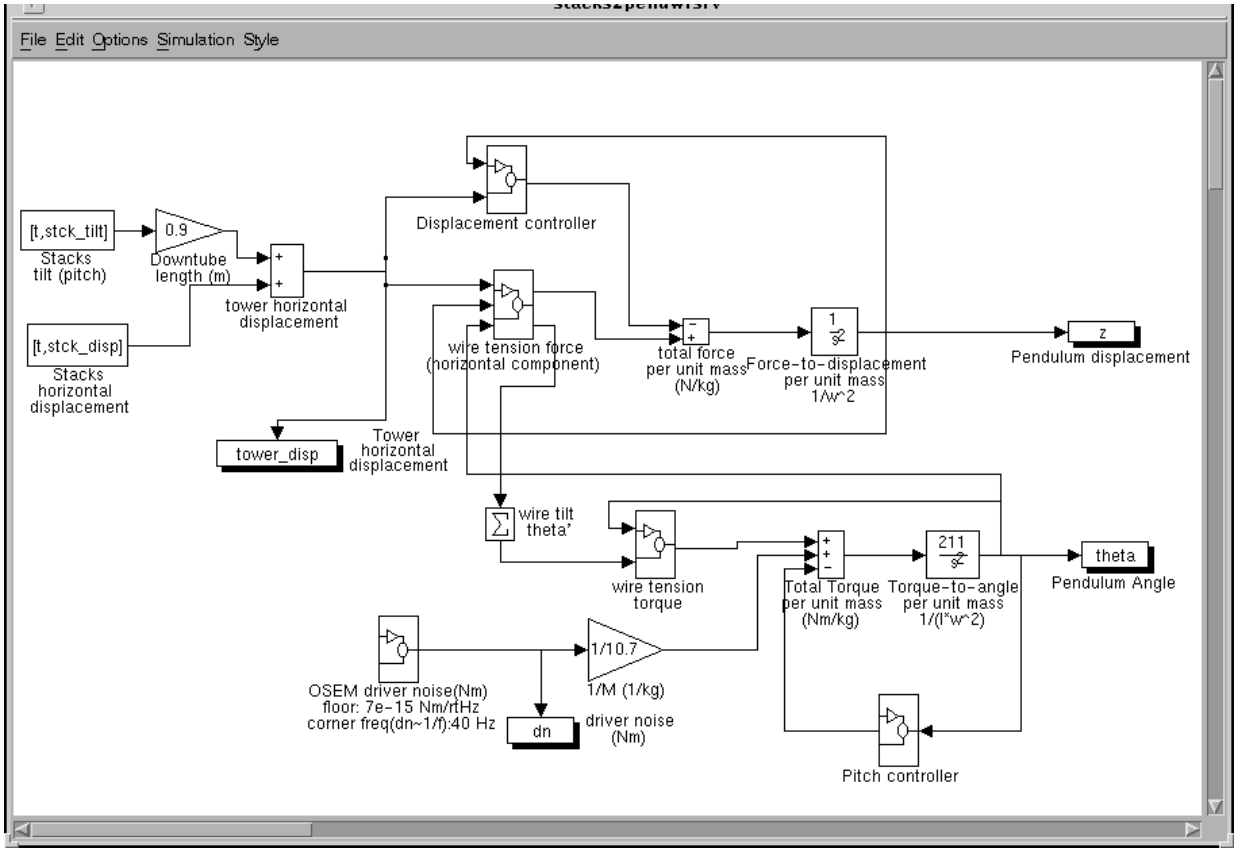

Figure 22 Block diagram for model of stack optic plate motion to pendulum motion.

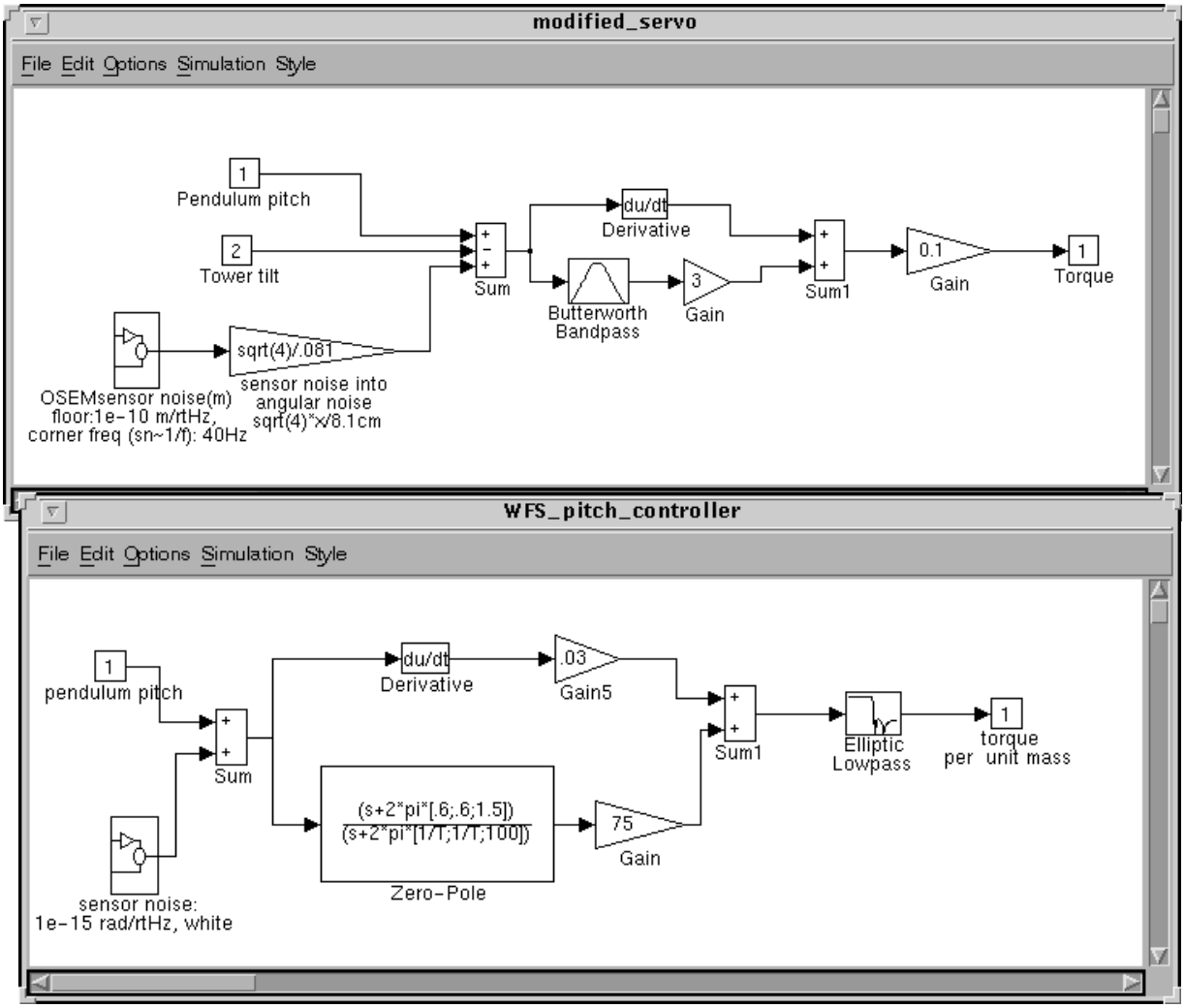

Figure 23 Block diagrams of pitch controllers. Top: Modified local damping servo, with increased gain at 0.15 Hz. Standard velocity damping is implemented by opening the Butterworth bandpass path and adding low-pass filtering - see reference [8]. Bottom: Controller for the WFS servo.

APPENDIX 4 ASC CHANNEL COUNT

The channel counts and characteristics for the ASC are given in Table 10 below.

	Channel	No.	Type	Category	from:	to:	Rate (Hz)	Comment
WPU	**Wavefront sensing; angular misalignment (per sensor):**							
	PD DC	4	input	16 bit ADC	WFS	WPU	65536	PD: photodiode
	PD down-conv.	8	input	16 bit ADC	WFS	WPU	65536	
	sampling clock	1	input	clock	DAQ	WFS	65536	GPS
	world time	1	input	num.	ISCC	WFS		for time stamps
	angle	2	internal	32 bit num.	WPU	ISCC	2048	**Alignment Data**
	LO RF	1	input	RF	LSC	WFS		LO: local oscillator
	LO phase	1	input	16 bit ADC	WFS	WPU	65536	looped from DAC
	LO phase	1	output	16 bit DAC	WPU	WFS	65536	
	gain switch	1	output	binary	WPU	WFS		–20dB RF gain
	cal. light switch	1	output	binary	WPU	WFS		shot noise calibration
	shutter status	1	input	binary	WFS	WPU		
	beam steering	1	output	RS232/GPIB	WPU	WFS		motorized mount (e.g. New Focus)

Table 10 ASC Channel Count

	Channel	No.	Type	Category	from:	to:	Rate (Hz)	Comment
IPU	**Image processing (per camera):**							
	TV signal	1	input	TV	camera	IPU		
	zoom	1	output	binary	IPU	camera		
	IR filter	1	output	binary	IPU	camera		
	illumination	1	output	binary	IPU	camera		on-off switch for light
	TV image	1	output	digital/analog	IPU	DAQ	1MB	576x385 pixels, 30 Hz
	beam parameters	5	internal	16 bit num.	IPU	ISCC	256	**Centering Data** (CoG, Γ, I, etc.)
	world time	1	input	num.	ISCC	WFS		for time stamps
QMPU	**Beam position and intensity monitor (per quadrant cell/monitor):**							
	PD quadrant	4	input	16 bit ADC	sensor	QMPU	65536	
	intensity monitor	1	input	16 bit ADC	sensor	QMPU	65536	
	sampling clock	1	input	clock	DAQ	QMPU	65536	GPS
	world time	1	input	num.	ISCC	QMPU		for time stamps
	X/Y/I	3	internal	32 bit num.	QMPU	ISCC	2048	**Beam Direction Data**

Table 10 ASC Channel Count

	Channel	No.	Type	Category	from:	to:	Rate (Hz)	Comment
OLPU	**Optical levers (per unit):**							
	PD quadrant	4	input	16 bit ADC	sensor	OLPU	65536	
	intensity monitor	1	input	16 bit ADC	sensor	OLPU	65536	
	sampling clock	1	input	clock	DAQ	OLPU	65536	GPS
	world time	1	input	num.	ISCC	OLPU		for time stamps
	Θ/Φ/I	3	internal	32 bit num.	OLPU	ISCC	2048	**Optical Lever Data**
	laser diagnostic	2	input	8 bit ADC	laser diode	OLPU	256	voltage/current
	laser diagnostic	1	internal	16 bit num.	OLPU	ISCC	32	
Miscellaneous	**Miscellaneous Sensors:**							
	beam direction	2	input	num.	IOO	ISCC	256	
	beam offset	2	input	num.	IOO	ISCC	256	
	beam intensity	1	input	num.	IOO	ISCC	2048	
	laser ok	1	input	num.	PSL	ISCC	256	
	modulation depth	2	input	num.	IOO	ISCC	256	
	remaining AM	2	input	num.	IOO	ISCC	256	
	telescope	2	input	num.	IOO	ISCC	1	mode matching parameters
	shadow detector	16	input	num.	SUS/COS	ISCC	256	**Suspension Data**
LPU	**Length sensing (interferometer lock acquisition only):**							
	length signals[a]	6	input	32 bit num.	LPU	ISCC	16384	**Length Data** (I/Q phase)
	PD DC[1]	3	input	32 bit num.	LPU	ISCC	2048	
	status signals	TBD	in/out	num.	LPU	ISCC		TBD

Table 10 ASC Channel Count

	Channel	No.	Type	Category	from:	to:	Rate (Hz)	Comment
Drivers	**Alignment Drivers:**							
	ifo angles	12	output	16 bit DAC	ISCC	SUS	2048	
	beam steering	4	output	16 bit DAC	ISCC	COS	2048	
	mirror transverse	6	output	num.	ISCC	SEI	manual	centering of ITMs/BS
	telescope	2	output	num.	ISCC	IOO	manual	mode matching input beam
	ifo length[1]	6	output	16 bit DAC	ISCC	LSC/SUS	16384	lock acquisition only
	sampling clock	1	input	clock	DAQ	driver DACs	65536	GPS
ISCC	**ISC Computer:**							
	Alignment Data	10	output	32 bit num.	ISCC	DAQ	2048	yaw and pitch
	Beam Direction D.	8	output	32 bit num.	ISCC	DAQ	2048	x and y
	Centering Data	12	output	32 bit num.	ISCC	DAQ	1	x and y
	Optical Lever Data	12	output	32 bit num.	ISCC	DAQ	2048	yaw and pitch
	ifo angles	12	output	32 bit num.	ISCC	DAQ	2048	
	beam steering	4	output	32 bit num.	ISCC	DAQ	2048	
	sampling clock	1	input	clock	DAQ	ISCC	1	watch dog
	world time	1	input	num.	DAQ	ISCC		absolute time reference
	ifo lock	1	output	binary	ISCC	Cons./LSC		status signal / trigger
	ASC Status	TBD	output	data records	ISCC	Cons./DAQ		includes servo parameters
	ASC Control	TBD	input	data records	ISCC	Console		

Table 10 ASC Channel Count

	Channel	No.	Type	Category	from:	to:	Rate (Hz)	Comment
MCC	**Mode Cleaner Computer:**							
	alignment data	4	input	32 bit num.	WPU	MCC	2048	MC only
	mirror angles	6	output	16 bit DAC	MCC	IOO	2048	MC only
	shadow detectors	6	input	num.	IOO	MCC	256	MC only
	laser ok	1	input	num.	PSL	MCC	256	
	beam intensity	1	input	num.	IOO	MCC	2048	
	modulation depth	1	input	num.	IOO	MCC	256	

Table 10 ASC Channel Count

a. Only implemented, if a combined ASC/LSC lock guiding system is required.

APPENDIX 5 REFERENCES

[1] LIGO-T950065-A-C01, *Detector Subsystems Requirements.*

[2] LIGO-T950072-00-R, *Evaluation of proposed changes to the suspension sensor electronics.*

[3] LIGO-T960005-00-R, *Principles of Calculating Alignment Signals in Complex Resonant Optical Interferometers.*

[4] LIGO-T960085-00-D, *LSC Configuration Issues*

[5] LIGO-T960065, *Seismic Isolation Design Requirements Document*, section 2.5.5.

[6] LIGO-T960103-00-D, *ASC: Environmental Input to Alignment Noise.*

[7] LIGO-T960111-A-D, *Wavefront Sensor.*

[8] LIGO-T960040-00-D, *Response of Pendulum to Motion of Suspension Point.*

[9] LIGO-E950090-00-E, and LIGO-L960256-00-E.